NASA Technical Paper 3033

January 1991

# Axisymmetric Shell Analysis of the Space Shuttle Solid Rocket Booster Field Joint

Michael P. Nemeth
and Melvin S. Anderson



NASA

**NASA Technical Paper 3033**

1991

# Axisymmetric Shell Analysis of the Space Shuttle Solid Rocket Booster Field Joint

Michael P. Nemeth
*Langley Research Center*
*Hampton, Virginia*

Melvin S. Anderson
*Old Dominion University*
*Norfolk, Virginia*

NASA
National Aeronautics and Space Administration
Office of Management
Scientific and Technical Information Division

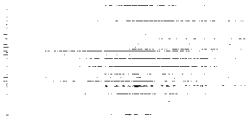

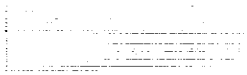

## Summary

The Space Shuttle *Challenger* accident (flight STS-51-L) led to an intense investigation of the structural behavior of the solid rocket booster (SRB) tang and clevis field joints. The presence of structural deformations between the clevis inner leg and the tang, substantial enough to prevent the O-ring seals from eliminating the flow of hot gas through the joints, has emerged as a likely cause of the vehicle failure. This paper presents results of axisymmetric shell analyses that parametrically assess the structural behavior of SRB field joints subjected to quasi-steady-state internal pressure loading for both the original joints flown on flight STS-51-L and the redesigned joints flown on the first flight after the accident (on the Space Shuttle *Discovery*). Axisymmetric shell modeling issues and details are discussed and a generic method for simulating contact between adjacent shells of revolution is described. Results are presented that identify the performance trends of the joints for a wide range of joint parameters. Results are also presented for several proposed modifications to the original joint that indicate alternate ways of reducing the relative displacements between the tang and the clevis inner leg. Finally, an assessment of the influence of the external tank attachment ring on the relative displacements between the tang and the clevis inner leg is presented.

An important finding of this study is that the redesigned joint exhibits significantly smaller O-ring gap changes and much less sensitivity to joint clearances than the original joint. Unlike the original joint, the redesigned joint exhibits practically the same size O-ring gap changes and behavior trends regardless of which O-ring seals the joint. For a wide range of joint parameters, the results presented in this study indicate that the redesigned joint provides a much better pressure seal than the original joint.

## Introduction

An intense effort has been underway at the NASA Langley Research Center since the loss of the Space Shuttle *Challenger* (flight STS-51-L) to study the structural behavior of the right solid rocket booster (SRB). Review of the evidence and facts leading up to the loss of the vehicle has focused on the failure of the aft (lower most) tang and clevis field joint of the right SRB as the probable cause of the accident (ref. 1). Structural analyses of this field joint have been performed on several levels at Langley (refs. 2 to 4) and at the NASA George C. Marshall Space Flight Center (ref. 5). These analysis levels range from simple axisymmetric shell analyses to very sophisticated three-dimensional inelastic finite-element analyses. The axisymmetric shell analyses were used to identify the qualitative joint behavior trends and to provide guidance for the more sophisticated analyses. This paper focuses on elastic axisymmetric shell analyses performed with the computer program FASOR (ref. 6) and contains an expanded account of the work presented in reference 2. Specifically, the paper describes modeling issues necessary to predict adequately the qualitative joint behavior trends and presents a generic methodology for parametrically simulating contact within the joint as a function of the initial joint clearances. The method presented herein allows very rapid calculations of joint response so that studies involving a large number of parameters are practical. This paper presents results that indicate the redesigned SRB field joint provides substantially improved performance over that of the original joint design.

Results are also presented in the appendixes for three modified SRB designs that use the original joint. The first design modification consists of the addition of exterior rings to the SRB on either the tang side or both sides of each field joint. The second design modification entails the placement of a small amount of shell wall eccentricity in the SRB on both sides of each field joint. Similarly, the third design modification entails the placement of kinks in the shell wall of the SRB on both sides of each field joint. All three of these SRB design modifications were investigated to determine if the longitudinal bending gradients in the SRB could be shifted away from the joint without inelastically deforming two adjoining motor cases. Moreover, these designs were considered as part of a preliminary effort to determine alternate ways of improving joint performance that use the original joint design and involve as little additional retooling as possible.

Results are also presented that indicate the influence of the external tank attachment (ETA) ring assembly on the relative displacements between the tang and the clevis inner leg. This ring assembly is located near the aft field joint, where the SRB failed on flight STS-51-L (ref. 1).

The authors wish to acknowledge J. H. Starnes, Jr., and W. Allen Walters, Jr., who directed the laboratory experiments.

## Symbols

| | |
|---|---|
| $d, d^*$ | radial distance between tang and clevis inner leg before and after motor pressurization (see fig. 10), in. |
| $\tilde{d}$ | shell wall taper location (see fig. 28), in. |

| | |
|---|---|
| $EA/S$ | smeared extensional stiffness of shell segment representing pin connection, lb/in. |
| $EI/S$ | smeared bending stiffness of shell segment representing pin connection, in-lb |
| $e$ | eccentricity (see fig. 27), in. |
| $F_j$ | contact force, $j = 1$ to 7 (see fig. 22), lb/in. |
| $G_j$ | radial distance between shell wall surfaces corresponding to $F_j, j = 1$ to 7 (see eq. (A1)), in. |
| $H$ | ring thickness (see fig. 24), in. |
| $H_0, H_1$ | dimensions of tang and clevis pin region (see fig. 4), in. |
| $l$ | shell wall taper length (see fig. 27), in. |
| $N$ | number of contact locations (see appendix A) |
| $p$ | pressure due to burning of solid propellant, psi |
| $S$ | pin spacing, in. |
| $s$ | exterior ring location (see fig. 23), in. |
| $t_1, t_2$ | dimensions of capture feature and clevis inner leg (see fig. 9(b)), in. |
| $\Delta$ | O-ring gap change (see fig. 10), in. |
| $\Delta_{ri}$ | radial displacement at point $r$ due to influence loads associated with contact force $F_i$ (see eq. (A1)), in. |
| $\Delta_{rp}$ | radial displacement at point $r$ due to unit pressure loading (see eq. (A1)), in. |
| $\Delta_{si}$ | radial displacement at point $s$ due to influence loads associated with $F_i$ (see eq. (A1)), in. |
| $\Delta_{sp}$ | radial displacement at point $s$ due to unit pressure loading (see eq. (A1)), in. |
| $\delta_j$ | initial joint clearance, $j = 1$ to 5 (see fig. 9), in. |
| $\mu$ | joint clearance defined by $\mu = t_1 - t_2 = \delta_4 + \delta_5$ (see fig. 9(b)), in. |

## Overview

The original and redesigned SRB field joints shown in figure 1 each consist of a male-to-female, pin-connected joint between two cylindrical shells referred to as solid rocket motor (SRM) cases. These SRM cases are approximately 12 ft in diameter and 30 ft long. The male and female parts of the joint are referred to as the tang and clevis, respectively. The parts of the clevis on the inside and outside of the cylinder are referred to as the inner and outer legs. The original joint uses two O-rings to provide a pressure seal between two SRM cases. The redesigned joint has an additional part on the tang, referred to as the capture feature, which is intended to limit the deflections between the tang and clevis inner leg. The redesigned joint is based on the original joint design concept with small differences in dimensions, the addition of the capture feature, and the presence of a third O-ring.

A total of 180 pins spaced equally around the joint circumference are inserted into holes that are machined through the tang and partially through the clevis (for both the original and the redesigned joint) as indicated in figure 1. The pins are held in place by a metal retainer strap on the outer surface of the joint. Metal shims are placed between the tang and clevis outer leg (clipped onto the pins) to reduce the initial joint clearance between the tang and the clevis inner leg. Rubber O-rings are used to provide a pressure seal during motor operation. The effectiveness of the O-rings in providing this seal depends on the relative displacements of the parts of the joint in the proximity of the O-rings. (See ref. 1.)

The Space Shuttle experiences a number of dynamic loading conditions prior to and during the 2-minute-long part of the ascent when the SRB's are operational. An important loading condition for the boosters that is addressed herein is the maximum quasi-steady-state internal pressure of approximately 1000 psi exerted on the shell wall by the burning of the solid propellant during vehicle ascent.

## Modeling Assumptions and Details

Two SRM cases joined together by either the original or the redesigned field joint possess periodic circumferential symmetry. It is possible to identify a basic repetitive meridional element of the joined SRM cases that possesses the same stiffness, loading, and support conditions when translated circumferentially by a finite angle. For the SRM cases, this angle is 2°. Since this angle is small, it appears reasonable to assume that the overall stiffness of the field joint can be matched closely enough by the axisymmetric analysis to represent adequately the structural behavior of the joint in the vicinity of the O-ring pressure seals.

The SRM field joint has several characteristics that must be considered when an axisymmetric shell analysis is used, especially when local joint behavior trends are the desired end result of the analysis.

These characteristics for the original joint are indicated in figure 2, and they lead to modeling issues that may significantly affect the analytical results. The issues that appear to be most important are the modeling of the pin connection (contribution of the pin stiffnesses to the shell model), the local stiffness reduction associated with the pinhole and the O-ring grooves, the internal pressure distribution near the O-rings, the way the load is transferred between the tang and clevis by the pin reaction forces, and the clearances between the tang, clevis, and pin. The SRM cases are fabricated from D6AC steel and the nominal material properties for this material used in the analyses are $E = 29 \times 10^6$ psi for Young's modulus and $\nu = 0.3$ for Poisson's ratio. The geometry and dimensions of the original and redesigned joints are given in figure 3.

### Local Stiffness Modeling Details

The tang is connected to the clevis by discrete pins that can only be modeled by continuous shell segments in a shell-of-revolution analysis. To simulate the actual three-dimensional flexibility of the joint as accurately as shell analysis will permit, the shell segments representing the pin are assumed to contribute only meridional stiffness to the joint model. This assumption is implemented in the FASOR model by elimination of the circumferential stiffnesses of the shell segments representing the pin connection. The meridional extensional and bending stiffnesses of the shell segments representing the pin are approximated by the smeared stiffnesses $EA/S$ and $EI/S$, where $S$ is the pin spacing and $EA$ and $EI$ are the extensional and bending stiffnesses of a pin, respectively.

The circumferential variation in stiffness of the shell due to the pinholes is approximated in a manner consistent with shell-of-revolution analysis through use of a reduced value of stiffness that is assumed to be constant around the circumference of the shell. The stiffness reduction associated with the pinholes is implemented in the FASOR model by introduction of a linear thickness variation over the pinhole region for the tang and both clevis legs. This region of thickness variation for the original joint and a typical element of the tang or the clevis legs are shown in figures 4(a) and 4(b), respectively. The linear thickness variation used in the FASOR models is determined from the requirement that the models have an average meridional bending stiffness that matches unpublished stiffness data determined in plate bending experiments performed at the NASA Langley Research Center. These experiments consisted of four-point bending tests of flat plates with hole diameters (nominally 1 in.) and hole spacings approximately the same as those of the SRM case field joint. These plate specimens were intended to represent the actual flight hardware to within the fidelity of the shell model. Stock plates were used in the experiments, with plate thicknesses that were close to the thicknesses of the actual tang and clevis legs. Holes were drilled completely through the plates used to simulate the tang and the clevis outer leg and partially through the plate intended to simulate the clevis inner leg. The depth of the holes drilled partially through the plate corresponded to the depth of the holes in the clevis inner leg. The experimental results indicated bending stiffness reductions due to holes in the clevis outer leg, the tang, and the clevis inner leg to be approximately 57, 63, and 58 percent, respectively. The dimensions of the linear thickness variations $H_0$ and $H_1$ used in the FASOR model of the pinhole region are depicted in figure 4(b). The dimension $H_0$ is predetermined by the dimensions of the tang and the clevis legs. The dimension $H_1$ is determined by analytically finding the thickness that produces the same bending stiffness reductions that were obtained in the experiments.

A reduced meridional stiffness for the clevis inner leg is implemented in the FASOR model to account for the fact that the O-ring grooves cannot have meridional stresses acting on their traction-free surfaces. The region where the stiffnesses are modified is assumed to cover the shaded region shown in figure 4(c). The FASOR program allows the input of orthotropic elastic moduli, and this convenience is used to selectively modify the stiffnesses of the O-ring grooves. The shaded region between the O-ring grooves is assigned an elastic modulus of zero in its meridional direction. The meridional stiffnesses of the remaining shaded regions shown in figure 4(c) are calculated with an elastic modulus in their meridional directions that varies from the full value to zero at the traction-free surfaces of the O-ring grooves. For all the shaded regions shown in figure 4(c) the full circumferential stiffness is retained.

### Local Pressure Distribution Modeling Details

The relative displacements between the tang and the clevis inner leg in the vicinity of the O-rings depend upon where the pressure seal actually occurs. The pressure distribution illustrated in figure 2 corresponds to one in which the pressure has been prevented from reaching the O-ring seals. This distribution corresponds to the factory assembly of two SRM cases in which a rubber liner totally seals the joint (referred to as a factory joint) and the pressure never reaches the O-rings. If the liner is not present, as is the case for the field joints, the pressure acts

on the tang and both sides of the clevis inner leg up to the next point of sealing. The pressure distributions corresponding to the primary O-ring sealing the joint and to the primary O-ring failing and the secondary O-ring sealing the joint are diagrammed in figures 5(a) and 5(b), respectively. The pressure seals provided by the O-rings are assumed in the FASOR model to occur at the center of the O-ring grooves. As previously mentioned, the redesigned joint contains an additional O-ring, referred to herein as the tertiary O-ring. The pressure distributions investigated in the analysis of the redesigned joint are shown in figures 6(a) through 6(c). In the redesigned joint, the tertiary O-ring is the first O-ring to encounter motor pressure. In figures 5 and 6, the bold line denoting the points of pressure application to the joint reflects the fact that when the pressure acts on both surfaces of a shell segment (as typically occurs on the clevis inner leg), the variation in pressure from one side of the shell segment to the other side is negligible within the limits of thin-shell theory.

### Pin-Tang-Clevis Load Transfer Modeling

The nominal internal pressure of 1000 psi generated by burning of the propellant induces an axial loading in the shell wall of 36 345 lb/in., which corresponds to the biaxial state of stress occurring in a sealed pressure vessel. This axial loading causes approximately 92 220 lb of axial force to be transferred by each pin. The load transfer between the tang, clevis, and pins occurs in a periodic manner because of the periodic occurrence of the pinholes, as indicated in figure 7. Moreover, the pins bear on the tang and clevis to produce a contact stress distribution within each pinhole. (See fig. 7.) The way in which the pins bear on the clevis inner leg, through the thickness of the shell, is depicted in figure 8. The shape of the through-the-thickness stress distribution generally depends on the amount of pin deformation, the clearances in the pinhole, the amount of beveling of the edges of the pin (see fig. 8(b)), the amount of friction between the pin, tang, and clevis, and any inelastic local deformations that result from high stresses. Associated with the contact stress distribution of a pin is a resultant pin bearing force. (See fig. 8(c).) The large size and the proximity of the resultant pin bearing force to the O-ring pressure seals suggest that the manner in which the pins bear on the clevis inner leg is an important modeling detail to be addressed.

Axisymmetric shell analysis cannot model the local three-dimensional nature of the periodic pin contact stresses inside the hole, but it can simulate the actual load transfer between the pin and the pinhole with a statically equivalent uniform load distribution. This simulation is accomplished by investigation of the sensitivity of the FASOR model to the location of the reference surface of the clevis inner leg. The length of the shell segment connecting the clevis inner leg to the tang depends on the location of the shell wall reference surface. Varying the length of this connecting shell segment changes its bending stiffness and indirectly changes the location of the resultant pin bearing force.

As previously discussed, the stiffnesses of the shell segments representing the pin are modified to include only meridional stiffness since the pin contributes essentially no circumferential stiffness to the joint. Joining the tang and clevis in this manner constrains the tang from sliding on the pin and corresponds to a no-slip connection between the tang, clevis, and pin. Preventing slippage between the tang, clevis, and pin was shown to be an important modeling issue of the SRM joint in reference 3.

## Clearances and Contact Modeling

The results of the referee tests of the original SRM field joint (ref. 7) indicate that initial clearances affect the relative displacements between the tang and the clevis inner leg at the O-rings. Ideally, it is desirable to know the effect of a wide range of clearances on the structural behavior of the field joint. This effect is studied through application of a contact analysis that uses an influence coefficient method in which pairs of loads are applied to assumed contact points on adjacent shell walls. This influence coefficient method can simulate contact between adjacent shell walls; however, it does not address clearances and contact between the pin, tang, and clevis legs. The locations and number of contact points required to sufficiently simulate the joint behavior were determined in the present study from examination of the joint deflections obtained from shell analyses of the joint in which adjacent shell walls were free to overlap one another. This effort led to the selection of points on adjacent shell walls as the contact points corresponding to locations A to C of the original joint (fig. 9(a)) and to locations A to G of the redesigned joint (fig. 9(b)). Associated with each contact point is an initial clearance indicated by $\delta_1$ to $\delta_5$ in figure 9. These clearances represent the radial distances between adjacent shell walls prior to assembly and pressurization of the joint. The clearance $\delta_1$ is particularly significant in that it corresponds to the shimming process applied to the joint during assembly. The values of $\delta_1$ investigated in this study include all shim sizes used in the referee tests and on the actual flight articles. Thus, the maximum value of $\delta_1$ corresponds to a joint without shims, and a zero value corresponds to a joint where the shimming process produces perfect contact between the adjacent shell

walls and results in no clearance. In this study, the remaining clearances, $\delta_2$ to $\delta_5$, are considered not to be explicitly defined by the joint assembly and shimming process performed on the joint. However, to obtain a broad picture of the importance of these clearances, the range of values of $\delta_2$ through $\delta_5$ investigated in this study was selected to be the same as the range of values considered for $\delta_1$.

The basic idea behind the contact analysis is to compute the forces at two assumed contact points that are necessary to prevent adjacent shell walls from overlapping. This task is accomplished by enforcing radial displacement compatibility between two assumed contact points when the deflections and clearances are such that contact occurs. The relative displacements between the tang and the clevis at the O-rings are then adjusted to reflect the presence of any contact forces. For a given set of clearances and $N$ possible contact locations, there exists $2^N$ possible contact conditions that can be determined by analysis. There is, however, only one physically admissible solution. This solution is found by excluding all solutions that produce tensile contact forces and inadmissible relative displacements (those that overlap) between adjacent shell walls. An algorithm was developed to determine the physically admissible solution. Details of the algorithm are given in appendix A.

## Results and Discussion

The effectiveness of the O-rings in providing a pressure seal inside the SRB's to eliminate hot gas flow through the SRM field joints depends heavily on the relative radial displacements between the tang and the clevis inner leg in the proximity of the O-rings. A specific relative displacement is used in this paper to assess the joint performance and represents the joint displacement that an O-ring must follow during motor pressurization to ensure safe operation. This displacement parameter is the relative radial displacement between the inner surface of the tang and the outer surface of the clevis inner leg midway between the primary and secondary O-rings, and it is illustrated in figures 10(a) and 10(b). This displacement results from motor pressurization and is important for both the original and the redesigned joint. After joint assembly, the radial distance (referred to herein as the gap) separating adjacent surfaces of the tang and the clevis inner leg between the primary and secondary O-rings is a specific amount denoted in figure 10(a) as $d$. Upon motor pressurization, the initial gap magnitude $d$ changes to a different gap magnitude $d^*$. (See fig. 10(b).) The relative radial displacement that the O-rings must follow to ensure a pressure seal is given by $\Delta = d^* - d$ and is referred to hereinafter as the O-ring gap change. Positive values of $\Delta$ represent greater separation of the tang and the clevis inner leg after motor pressurization, whereas negative values indicate the tang and the clevis inner leg are closer together after motor pressurization.

In subsequent sections, results are presented for the original joint, for the redesigned joint, and for the influence of the external tank attachment ring on the redesigned joint. In the early phases of the study, modified SRB designs that use the original joint were also investigated. These design modifications are shown in figure 11, and corresponding results are presented in appendixes B and C. The results presented in these appendixes and in the following sections of this paper indicate that the modified SRB designs are not viable means of improving the performance of the original joint compared with the performance of the redesigned joint. Thus, the discussion of these results has been excluded from the main body of the paper.

### Results for the Original Joint

The initial FASOR linear analysis of the original SRM joint yielded O-ring gap changes ranging from 0.021 to 0.026 in. This range of gap changes was obtained for clearances $\delta_1$ and $\delta_2$ from 0 to 0.050 in. and a nominal value of $\delta_3$ equal to 0.050 in. (See fig. 9(a).) Similar analyses performed with three-dimensional finite-element analysis are presented in references 3 to 5. The results presented in these references indicate O-ring gap changes varying from approximately 0.019 to 0.037 in. The variation in the O-ring gap changes reported in references 3 to 5 is attributed primarily to differences in local modeling details and clearances (three-dimensional effects) around the pin and pinhole region, in addition to smaller contributions due to clearances between the tang and the clevis. The smaller O-ring gap change (0.019 in.) corresponds to the ideal case of a joint with a perfectly fitting pin, a value of $\delta_1 = 0$, and zero initial clearance between the tang and the clevis inner leg in the vicinity of the O-rings. Moreover, the results presented in reference 3 indicate that varying the clearance between the tang and the clevis inner leg in the vicinity of the O-rings from 0 to 0.015 in., while maintaining $\delta_1 = 0$, produces a maximum increase in O-ring gap change of approximately 0.004 in. Parametric studies of the effects of $\delta_2$ and $\delta_3$ were not included in the finite-element analyses, and the particular values used in the models are not indicated in references 3 to 5. Comparison of the range of the initial FASOR results (0.021 to 0.026 in.) with the magnitude of the finite-element results for a perfectly fitting pin (0.019 to 0.023 in.) suggests that the

FASOR model is capable of capturing the fundamental effects of clearances between adjacent shell walls of the tang and the clevis on the joint performance.

The FASOR and finite-element results previously described indicate that axisymmetric shell analysis cannot simulate exactly the local three-dimensional aspects of the pin region such as clearances and pin-edge bevel. (See fig. 8.) The pin connection is treated as an ideal connection in the shell analysis. However, this ideal connection can be tuned somewhat to improve the idealized simulation of the load transfer between the tang, the clevis, and the pin. One modeling parameter that can be adjusted in the shell analysis to perform this task is the location of the reference surface of the clevis inner leg. This parameter determines the length of the shell segment connecting the clevis inner leg to the tang, and hence it affects its bending stiffness and indirectly determines the location at which the statically equivalent pin reaction force is transferred to the clevis inner leg, as indicated in figure 8. Results obtained for several different reference surface locations indicate that moving the reference surface from the innermost side of the clevis inner leg toward the tang results in only minor differences in the computed O-ring gap change and in a slight reduction in the sensitivity of the gap changes to the initial clearances $\delta_1$ and $\delta_2$. The largest variation in O-ring gap changes, associated with varying the initial clearances, is from 0.016 to 0.023 in. and corresponds to a reference surface located at the inner surface of the clevis inner leg. (See fig. 8.) Because of the fairly benign influence of reference surface location on the O-ring gap changes, a single reference surface location was used to perform the remaining parametric studies. This reference surface location is approximately at the midpoint of the partially drilled-through pinhole (0.3185 in. outboard from the interior surface of the clevis inner leg). In addition, the effect on the O-ring gap change of varying the initial clearance $\delta_3$ is benign and was eliminated as a parameter in the study of the original joint.

The O-ring gap changes recorded in the referee tests (ref. 7) range from 0.020 to 0.041 in., depending on circumferential location around the joint and the size of the shims used. The gap changes recorded were obtained from a pressure loading approximately 1 percent higher than the nominal 1000-psi pressure loading used in the analysis presented herein and in references 3 and 4. The results of reference 5 correspond to the same value of pressure as that used in the referee tests, (i.e., 1004 psi). The presence of a substantial variation in joint and pin clearances around the circumference of the shell was noted in the experiment. Specifically, measurements made on the tang and the clevis prior to testing indicate that clearances between the tang and both clevis legs, in the proximity of the O-rings, varied from 0.035 to 0.065 in. around the circumference of the shell. These clearances correspond to values of $\delta_1$ from 0 to approximately 0.030 in. for the shim sizes used in the referee tests.

The results of the initial FASOR analyses, the three-dimensional finite-element analyses, and the referee tests are presented in figure 12. The results shown for the FASOR analyses correspond to O-ring gap changes obtained by varying the clearances $\delta_1$ and $\delta_2$ from nominal values of 0 to 0.050 in. The results shown for the three-dimensional finite-element analyses range from gap changes corresponding to an ideal joint with a perfectly fitting pin (described above) to larger gap changes corresponding to additional flexibility associated with the pin, pin-edge bevel, and initial clearances (primarily clearances around the pin). The results shown for the referee tests were affected by small amounts of local plasticity in the vicinity of the pin connections in addition to joint clearances and exhibit slightly nonlinear behavior according to reference 7. The FASOR analyses indicate stresses in excess of the yield stress in the pin-connection region of the shell-of-revolution model. However, since the areas of plasticity indicated by the shell-of-revolution analyses are in the relatively small region of the joint where thicknesses were tapered to simulate the reduced bending stiffness of the pinholes, it is considered unrealistic to include plasticity in the axisymmetric analyses since the actual area of plastic deformation is in the localized pin bearing area.

The results of figure 12 show that both the FASOR analyses and the three-dimensional finite-element analyses yield O-ring gap changes that are in the range of the experimental results. Moreover, the results of the FASOR analyses and the three-dimensional finite-element analyses are in good agreement when the joint is assumed to have a perfectly fitting pin. The maximum O-ring gap change for the three-dimensional finite-element analyses agrees well with that for the referee tests and indicates that modeling of pin clearances, pin-edge bevel, and pin deformations is needed to predict accurately the behavior trends associated with these quantities. The results indicate that the FASOR analysis cannot predict the joint behavior accurately when three-dimensional effects associated with the pin are important. However, the good agreement between results for the FASOR analyses and those for the three-dimensional finite-element analyses for a joint with a perfectly fitting pin and the presence

of these results in the range of the experimental data reinforce the notion that the FASOR model is capable of capturing the fundamental effects of clearances between adjacent shell walls of the tang and the clevis on the joint performance. In addition, the relative simplicity of the FASOR analysis suggests that the axisymmetric shell analysis presented herein is useful for identifying structural trends of the SRM joints for a large range of parameters in a timely and relatively inexpensive manner.

Results obtained from the FASOR analyses and from the referee tests showing the sensitivity of the O-ring gap changes to local pressure distribution near the O-rings and to initial clearances are presented in figure 13. The parameter $x$ shown in this figure is the distance measured from the tip of the clevis inner leg toward the pin and is used to indicate the point at which the pressure distribution changes from being applied to the tang to being applied to the clevis inner leg. The band of results in figure 13 obtained from the FASOR analyses corresponds to clearances ranging from $\delta_1 = \delta_2 = 0$ to 0.050 in. and includes results for all clearances between these bounding values. These results indicate that preventing the pressure from reaching the O-rings (as in the case for the factory joints) produces the smallest O-ring gap changes for the full range of joint clearances. As $x$ increases to values that correspond to the locations of the centers of the primary and secondary O-rings, the ranges of O-ring gap changes increase to 0.021 to 0.026 in. and 0.031 to 0.036 in., respectively. The referee test results indicate the same trend as the FASOR results, but with somewhat larger O-ring gap changes and data scatter because of the added flexibility associated with the variation in clearances and the presence of plasticity, slight geometric nonlinearity, and slightly higher operating pressure.

The nonlinear static response of the joint was also determined as a function of the initial joint clearances. The nonlinear contact solutions were obtained by applying the incremental procedure described at the end of appendix A. This procedure converges rapidly and thus indicates a very slight, and essentially benign, influence of geometric nonlinearity on the O-ring gap changes. Because of the benign influence of geometric nonlinearity in the FASOR analyses and also reported in the referee tests, the remaining analyses presented herein for the original and redesigned joints neglect geometric nonlinearity.

### Results for the Redesigned Joint

The results presented in figures 14 to 16 show the effects of initial clearances on the O-ring gap changes for the redesigned joint. In particular, the results presented in figures 14 to 16 show the O-ring gap changes as a function of the clearance $\delta_4$ for the cases when the primary O-ring seals the joint, when the secondary O-ring seals the joint, and when the tertiary O-ring seals the joint. A band of results is shown in these figures that corresponds to O-ring gap changes for clearances from $\delta_1 = \delta_2 = 0$ to 0.050 in. and includes combinations of clearances between these bounding values. Results obtained for $\delta_3 = 0$ and 0.050 in. indicate no significant effect of varying $\delta_3$. Results for the original joint (independent of $\delta_4$) are included in figures 14 and 15 to highlight the advantage of the redesigned joint.

Another important parameter appearing in figures 14 to 16 is the clearance $\mu$. This clearance is defined as the difference between the width of the channel that the clevis inner leg slides into ($t_1$ in the figures) and the width of the clevis inner leg ($t_2$ in the figures). Moreover, the clearance $\mu$ is also the sum of the clearances $\delta_4$ and $\delta_5$, as indicated in figure 9(b). However, to simplify matters, the clearance $\delta_5$ is defined to be a dependent parameter, whereas the clearances $\mu$ and $\delta_4$ are defined as independent parameters. A value of $\mu = 0$ implies a perfect metal-to-metal assembly of the clevis inner leg and the capture feature with no clearance on either side of the clevis inner leg. This type of assembly would be very difficult to perform without damaging the O-rings in the joint, and results are included herein to indicate the effect of reducing $\mu$. In addition, the perfect metal-to-metal fit is considered to not provide a pressure seal. The nominal value of $\mu$ that is assumed to be representative of the actual flight hardware assembly is 0.020 in. in the present study.

The most important parameter used in the design of this joint is the clearance $\delta_4$. Positive values of $\delta_4$ correspond to a relative positioning of the capture feature and the clevis inner leg, prior to assembly, such as that depicted in figure 17(a). In this case, no contact is made between the outer surface of the capture feature (surface facing the outside of the shell) and the inner surface of the clevis inner leg when the joint is assembled. (See fig. 17(b).) For joints with $0 < \delta_4 \leq \mu$, the relative positioning of the tang and the clevis inner leg results in no contact between the clevis inner leg and either the capture feature or the tang when the joint is assembled. In this case, the joint exhibits the largest O-ring gap changes and behaves in a manner similar to that of the original joint; that is, the O-ring gap changes are determined by the relative stiffnesses of the tang and the clevis and are not influenced by any preloading because of an interference fit assembly. For joints with large values of $\delta_4$ (greater than $\mu$), the relative positioning of the tang and the clevis inner leg causes contact between the inner surface of the tang and the

outer surface of the clevis inner leg when the joint is assembled. After assembly, the clevis inner leg and the tang are deformed so that they tend to remain in contact when subjected to motor pressurization. This behavior is represented in figures 14 to 16 by the reduction in the O-ring gap changes as $\delta_4$ becomes greater than $\mu$. The increased force holding the clevis inner leg against the tang, associated with the increase in $\delta_4$, causes the reduction in the O-ring gap changes. However, as $\delta_4$ increases beyond $\mu$, the likelihood of damaging the primary and secondary O-rings during joint assembly also increases. This damage is undesirable since these O-rings constitute the primary sealing mechanism of the joint.

Negative values of $\delta_4$, referred to herein as an interference fit, correspond to a relative positioning of the capture feature and the clevis inner leg, prior to assembly, such as that shown in figure 18(a). With an interference fit, the tertiary O-ring in the capture feature is locked against the inner surface of the clevis inner leg and does not move during motor pressurization. (See fig. 16.) However, because of the possibility of damage to the tertiary O-ring during motor assembly associated with an interference fit, the tertiary O-ring seal is not relied upon as a primary sealing mechanism in the redesigned joint. After joint assembly, the capture feature and the clevis inner leg are deformed so that they remain in contact when the joint is pressurized, as indicated in figure 18(b). The results in figures 14 to 16 indicate that this deformed state has the positive effect of allowing only very small O-ring gap changes when the joint becomes pressurized.

Results of similar parametric studies of the redesigned joint involving substantially fewer joint parameters and obtained with three-dimensional finite-element analyses are presented in references 3 to 5. More specifically, these references show the effects of the clearance $\delta_1$ associated with the prelaunch shimming process, the capture feature clearance $\delta_4$, and the pressure seal location on the O-ring gap changes. Typically, the three-dimensional finite-element analyses yielded much larger O-ring gap changes than the FASOR analyses, but both analyses indicate the same trends. The larger gap changes obtained from the finite-element analyses are attributed to the more accurate three-dimensional flexibility of the finite-element models and the inclusion of clearances around the pin connection that are not included in the shell analysis presented here. The qualitative agreement between the FASOR results for the joint with a perfectly fitting pin and the three-dimensional finite-element results for the joint without a perfectly fitting pin reinforces the notion that the FASOR analysis adequately represents the effects of clearances between adjacent shell walls on the joint behavior. The pertinent results presented in references 3 to 5 are reproduced in figures 14 and 15 for comparison with results from the present study.

The results of the present study shown in figures 14 to 16 indicate that the redesigned joint has essentially the same behavior for the three pressure seal conditions; that is, the O-ring gap changes are about the same (less than 0.020 in.) for all three pressure seal conditions. Furthermore, these gap changes are substantially smaller than those of the original joint and thus do not require as large relative displacements for the O-rings to follow in the event of a pressure seal loss. One factor contributing to the improved performance of the redesigned joint is the reduction in the mismatch in circumferential stiffness of the tang and of the clevis because of the addition of the capture feature. In addition, the results of the present study shown in figures 14 to 16 indicate that the interference fit ($\delta_4 < 0$) yields substantially smaller O-ring gap changes in most cases than the fit with positive values of $\delta_4$ and exhibits much less sensitivity to variations in the clearances $\delta_1$ and $\delta_2$. The results from the three-dimensional finite-element analyses presented in references 3 to 5, and shown in figures 14 and 15, also indicate that joints with an interference fit exhibit O-ring gap changes substantially smaller than those of the original joint. Both the results of the present study and the results of references 3 to 5 indicate that the size of the O-ring gap change is essentially independent of the amount of interference between the capture feature and the clevis inner leg for all three pressure seal conditions. O-ring gap changes of 0.0052 and 0.0062 in. for an interference fit with pressure seals at the primary and secondary O-rings, respectively, are reported in references 3 and 4. These results correspond to clearances of about $\mu = 0.010$ in. and $\delta_1 = 0.007$ in. O-ring gap changes of between 0.0043 and 0.0058 in. are reported in reference 5. (See fig. 14.) These results correspond to joints with various interference fits and a pressure seal at the primary O-ring for which $\mu = 0.009$ in. and $\delta_1 \approx 0.010$ in. The results presented in reference 5 for $\delta_4 = 0$ in. ($\mu = 0.009$ in.) also indicate the O-ring gap changes are slightly sensitive to the clearance $\delta_1$. The results of reference 5 for joints with $\delta_4 = 0$ in. and $\delta_1$ varying between 0 in. and approximately 0.030 in. are shown in figures 14 and 15.

The results of the present study shown in figures 14 to 16 also indicate that reducing the clearance $\mu$ results in only slight reductions in the O-ring gap changes for joints with an interference fit. In contrast, figures 14 to 16 indicate that reducing the clearance $\mu$ results in substantially reduced O-ring gap changes and reduced sensitivity to clearances

for joints having positive values of clearance $\delta_4$. However, it should be reiterated that reducing the clearance $\mu$ increases the possibility of damaging the O-rings during motor assembly and losing the pressure seal altogether. The results presented in figures 14 to 16 indicate that an interference fit is practically insensitive to the clearance $\mu$ and yields small O-ring gap changes, and these findings suggest that it is an attractive joint design.

In the design of the original and redesigned joints, the primary and secondary O-rings constitute the primary sealing mechanism of the joint. Thus, the relative displacements of the tang and the clevis inner leg between the primary and secondary O-rings (O-ring gap changes) have been identified as the key parameter used for assessing the joint performance. However, when the tertiary O-ring seals the joint, the relative displacements between the capture feature and the clevis inner leg at the tertiary O-ring are also of interest. These relative displacements, referred to as the gap changes at the tertiary O-ring, are used in this study to indicate the nature of a pressure seal at the tertiary O-ring.

Results are also presented in figure 16 that indicate the gap changes at the tertiary O-ring as a function of the joint clearances for the case when the tertiary O-ring seals the joint. For $\delta_4 \leq 0$, there are no gap changes at the tertiary O-ring for the entire range of clearances considered. For $\delta_4 > 0$ and $\mu = 0.020$ in., the gap changes at the tertiary O-ring are such that the O-ring is compressed when the SRM becomes pressurized. As $\delta_4$ becomes greater than 0.020 in., the increase in force holding the clevis inner leg against the tang (associated with interference between the tang and the clevis inner leg at assembly) tends to reduce the gap change at the tertiary O-ring. This action relaxes the compression of the tertiary O-ring. Reducing $\mu$ has no effect on the gap changes at the tertiary O-ring for joints having an interference fit (i.e., negative values of $\delta_4$). However, reducing $\mu$ results in a change from O-ring compression to a small O-ring expansion for joints having positive values of $\delta_4$. This change in behavior is because for $\mu = 0$, small increases in $\delta_4$ result in substantial increases in the force (associated with an interference assembly of these two members of the joint) holding the tang and the clevis inner leg together.

An important result in figures 14 to 16 is the indication that because of the presence of the capture feature the redesigned joint behaves essentially the same whether the primary, secondary, or tertiary O-ring provides the pressure seal. This result is substantiated by both the shell analyses presented herein and the three-dimensional finite-element analyses presented in references 3 to 5. The similar behavior of the redesigned joints for each pressure seal case means, for instance, that if the primary O-ring fails to seal the joint, then the secondary O-ring only has to undergo small displacements to reseal the joint. This attribute of the redesigned joint, particularly for an interference fit (in which the O-ring gap change is essentially insensitive to changes in $\delta_4$), is a significant improvement over the original joint, in which the size of the O-ring gap change increases by a factor of 2 when the pressure seal moves from the primary O-ring to the secondary O-ring. The results shown in figure 16 for a joint with $\mu = 0.020$ in. (approximately the same clearance of the actual flight article) also suggest that if the tertiary O-ring seals the joint, then the joint is likely to remain sealed by the tertiary O-ring. However, the motor cases are 12 ft in diameter and are not perfectly circular to within very small tolerances. Thus, after assembly, the actual flight article may be operating over the entire spectrum of the results presented in figures 14 to 16 for various circumferential locations.

### Influence of External Tank Attachment Ring on Redesigned Joint

The external tank attachment (ETA) ring depicted in figure 19 is a built-up structure that is used to connect the aft end of a solid rocket booster (SRB) to the external fuel tank of the Space Shuttle. This built-up ring assembly is nonuniform around the circumference of the SRB and is connected by bolts to two axisymmetric stub rings that are part of the aft SRM case. The geometry of the ETA ring at its largest cross section and the geometry of the stub rings are shown in figure 20. Near the two stub rings, the shell wall of the aft SRM case is thicker than the nominal wall thickness of 0.4790 in. The top cover plate of the ETA ring consists of a series of circumferentially discontinuous plates that are bolted to two smaller rings shown in figure 20.

The main event that led to the loss of flight STS-51-L was the failure of the aft field joint of the right SRB (ref. 1). The aft field joint is located approximately 13.5 in. above the ETA ring assembly, as indicated in figure 19. Because of the proximity of the aft field joint to the ETA ring assembly, analyses were performed to determine the influence of the ETA ring on the O-ring gap changes.

As a first step in assessing the importance of the ETA ring assembly on the aft field joint, a FASOR model of the ring assembly with 30 in. of SRM shell wall on both sides of the stub rings was investigated. The axisymmetric FASOR model consisted of shell segments with the size and shape of the ETA ring cross section shown in figure 20. The nominal 1000-psi pressure loading discussed previously was applied

to the shell. Analyses were performed with FASOR models having full and reduced cover plate circumferential stiffnesses. The full and reduced cover plate stiffnesses are intended to serve as upper and lower bounds, respectively, on the behavior of the actual ETA ring, which has circumferentially discontinuous cover plates. The reduced cover plate stiffness is obtained by reduction of the circumferential modulus of elasticity of the shell wall comprising the cover plate by several orders of magnitude. This stiffness reduction is intended to simulate the lack of circumferential compatibility of the ETA ring cover plates in an averaged manner consistent with shell-of-revolution analysis. Geometrically nonlinear analyses were also performed for models with both cover plate stiffnesses to determine whether or not the additional flexibility associated with nonlinear displacements is important.

Figure 21 presents results that show the variation in meridional bending moment with axial distance from the end of the shell wall to the first stub ring. These results show that the linear and nonlinear analysis curves attenuate to a steady-state value at about the same rate, but slightly out of phase. The results also indicate that the differences in the meridional moment for the two cover plate stiffnesses are negligible for distances larger than approximately 5 in. away from the ring assembly. These results suggest that the differences in meridional moments for the two cover plate stiffnesses are fully attenuated before reaching the aft field joint and the differences in cover plate stiffnesses do not influence the behavior of the aft field joint.

To determine the importance of the attenuation phase shift in the meridional moments, obtained from linear and nonlinear analyses, on the behavior of the aft field joint, a FASOR model consisting of the redesigned joint combined with the ETA ring assembly was constructed. Results were obtained from this model for a joint having capture feature clearances of $\delta_4 = -0.020$ in. and 0.020 in. with $\delta_1 = 0$, $\delta_2 = 0$, and $\mu = 0.020$ in. The pressure seal was taken to be at the tertiary O-ring. The results obtained from the FASOR analyses for the two capture feature clearances considered indicate that the axisymmetric ETA ring assembly does not influence the O-ring gap changes of the aft field joint. Similar results obtained from linear and nonlinear analyses for the redesigned joint without the ETA ring assembly are nearly identical to the results corresponding to the joint with an axisymmetric ring of full depth. These results suggest that the circumferentially nonuniform ETA ring used on the actual flight article may have very little influence on the aft field joint when subjected to motor pressurization loading.

## Concluding Remarks

Results of axisymmetric shell analyses have been presented for the original and redesigned Space Shuttle solid rocket booster field joints and for three design modifications that use the original joint (see appendixes). The results were obtained with the shell-of-revolution computer code known as FASOR. Details of the modeling issues, a generic method for simulating contact in the joint, and the way in which the shell analysis treats these modeling issues have been discussed. Results of an in-depth parametric study of the structural behavior of the joints as a function of initial clearances have been presented. Comparisons of the axisymmetric shell analyses with experimental results and with three-dimensional finite-element analyses have also been presented for a few joint parameters. These comparisons indicate that the results of the present shell analyses agree well qualitatively with the experimental results and with the results of the three-dimensional finite-element analyses and can be used to identify the structural response trends to serve as a guide for more detailed three-dimensional finite-element analyses.

A wide range of parametric results for the original joint have been presented that indicate how the radial distance (referred to herein as the O-ring gap change) separating adjacent surfaces of the tang and the clevis inner leg between the primary and secondary O-rings changes as a function of initial clearances, pressure seal location, and geometric nonlinearity. These results indicate that substantial increases occur in the O-ring gap changes when the primary O-ring fails and the secondary O-ring then seals the joint. These results also indicate a benign effect of geometric nonlinearity on the O-ring gap changes and a moderate sensitivity of the O-ring gap changes to initial joint clearances.

A wide range of parametric results that indicate its behavior as a function of initial clearances and pressure seal location have also been presented for the redesigned joint. These results indicate that the addition of the capture feature to the redesigned joint significantly reduces the O-ring gap changes and the sensitivity to joint clearances compared with those of the original joint. In addition, the results show that, unlike the original joint, the redesigned joint exhibits practically the same O-ring gap changes and behavior trends regardless of which O-ring seals the joint. Furthermore, the results indicate that the interference fit configuration provides a good pressure seal. However, using an interference fit increases the likelihood of damaging the tertiary O-ring seal.

Results have also been presented that indicate the influence of the external tank attachment ring assembly on the redesigned field joint. The results indicate that the bending deformations associated with the pressurization of the shell wall at the external tank attachment ring have no effect on the local deformations of the redesigned joint.

Parametric studies of solid rocket motor cases joined together with the original joint and modified by either placing external rings on the cases, machining an eccentrically located joint in the cases, or machining a kink in the shell wall adjacent to the joint are also presented in the appendixes of this paper. These results indicate that the three design modifications to the original solid rocket booster design are effective means of reducing the O-ring gap changes but typically do not perform as well as the redesigned joint. The results also indicate that these three design modifications give rise to stresses in the shell wall that exceed the yield stress of the material, and thus they are not attractive as solid rocket booster designs.

NASA Langley Research Center
Hampton, VA 23665-5225
October 19, 1990

## Appendix A
## Contact Modeling Details

The basic FASOR models of the original and redesigned SRM joints do not account for contact between adjacent shell segments during structural deformation. Specifically, adjacent shell segments are free to overrun one another for certain loadings and initial clearances. To rectify this deficiency in the basic shell analysis, an influence coefficient method is used in conjunction with the FASOR models to obtain contact forces that prevent overrun of adjacent shell segments and hence provide more accurate physical models of the SRM joints. The general contact simulation procedure is identical for the original and the redesigned joint and is illustrated in this section only for the redesigned joint.

The influence coefficient method presented herein is based on the application of pairs of self-equilibrating loads, referred to hereinafter as influence loads, to points on adjacent shell segments that could come into contact with one another during deformation. There are assumed to be 7 locations involving 11 points on the shell where contact could occur with associated contact forces $F_1$ to $F_7$, as indicated in figures 22(a) to 22(d). Pairs of influence loads are applied in separate FASOR runs to determine the influence coefficients $\Delta_{ri}$, which are defined as the deflection of point $r$ due to the influence loading associated with $F_i$. The influence loads are inversely proportional to the radii of adjacent shell walls in order to satisfy the force equilibrium of adjacent differential elements of the two shell walls. Influence coefficients $\Delta_{rp}$ are also determined for a unit pressure loading on the shell. If $\delta_j$ is the initial gap between adjacent shell wall surfaces (i.e., the radial distance between adjacent shell wall surfaces before assembly and loading), the final gap $G_j$ after assembly and loading is given by

$$G_j = p\left(\Delta_{rp} - \Delta_{sp}\right) + \sum_{i=1}^{N} F_i\left(\Delta_{ri} - \Delta_{si}\right) + \delta_j \qquad \text{(A1)}$$

where the subscript $j$ ranges from 1 to $N$, the number of contact locations. The subscripts $r$ and $s$ represent two adjacent contact points associated with the contact forces $F_i$ shown in figure 22. The multiplier $p$ is used to specify the intensity of the actual pressure loading under consideration. Setting $p = 0$ corresponds to contact forces produced by joint assembly. Because of the proximity of certain locations, the number of clearance parameters used in the study was reduced by requiring that $\delta_6 = \delta_4$ and $\delta_7 = \delta_5$. In addition, the parameters $\delta_4$ and $\delta_5$ should not be considered to be completely independent. The independent parameter $\mu = \delta_4 + \delta_5$ has been introduced to better reflect the possible geometry of the joint. In this definition of $\mu$, the clearance $\delta_4$ is defined to be an independent parameter also, and the clearance $\delta_5$ is predetermined from specified values of $\mu$ and $\delta_4$. Positive values of $\mu$ indicate clearance between the capture feature and clevis inner leg, while negative values indicate that the clevis inner leg is larger than the channel formed by the capture feature that the clevis inner leg slides into.

Setting all the gaps $G_j$ equal to zero and solving equation (A1) for $F_i$ gives the contact forces at all the assumed contact points. In general, however, some of the contact forces are negative, an indication that a tensile force is required for displacement compatibility. This solution is not physically admissible. A physically admissible solution to equation (A1) is one in which all the contact forces $F_j$ $(j = 1, 2, \ldots, N)$ are either positive or zero and the gaps $G_j$ are zero for the locations with positive $F_j$ and are positive for the locations with zero values of $F_j$. A negative value of $G_j$ indicates that two adjacent surfaces have overrun each other. Thus, negative values of $G_j$ are physically inadmissible. Computationally, this process corresponds to eliminating the equations and contact forces associated with points not in contact from equation (A1). This elimination step is performed with the information about points not in contact used to define a pivotal strategy in a Gaussian elimination subroutine.

The unique contact solution may be found by considering all possible combinations for $F_j = 0$ in equation (A1), solving the reduced set of equations obtained by including only those with $F_j \neq 0$, and then calculating $G_j$ for the locations having $F_j = 0$. If $N$ is the number of pairs of possible contact locations that may be either open or closed, there are $2^N$ total contact combinations that must be considered. The analysis of all the various load combinations is facilitated by considering the $2^N$ binary numbers from 0 to $2^N - 1$. Each digit in the binary number is assigned to one of the locations and the load at that location is taken to be zero or nonzero according to whether there is a 0 or a 1 in that particular digit of the binary number. For 7 possible contact locations ($N = 7$), there are 128 combinations that need to be considered: 1 combination taking 7 values of $F_j$ at a time, 7 combinations taking 6 values of $F_j$ at a time, 21 combinations taking 5 values of $F_j$ at a time, 35 combinations taking 4 values of $F_j$ at a time, 35 combinations taking 3 values of $F_j$ at a time, 21 combinations taking 2 values of $F_j$ at a

time, 7 combinations taking 1 value of $F_j$ at a time, and 1 combination taking 0 values of $F_j$ at a time (no contact). Because this is a physical problem that has a unique solution, only one of these combinations satisfies all the required conditions. Solutions for the original SRM joint are obtained from consideration of only the three equations of equation (A1) corresponding to $F_1$, $F_2$, and $F_3$. All seven values of $F_j$ are considered for the redesigned joint.

The nonlinear solutions for the original and redesigned joints were obtained with the contact formulation previously described. First, a linear solution is obtained from which the values and locations of the nonzero contact forces are obtained. The nonzero contact forces are then applied to the FASOR model in addition to the motor pressure loading, and a nonlinear analysis is performed. From the nonlinear analysis new displacements $\tilde{\Delta}_{rp}$ and $\tilde{\Delta}_{sp}$ are obtained. The displacements $\tilde{\Delta}_{rp}$ and $\tilde{\Delta}_{sp}$ are then substituted into equation (A1) for $\Delta_{rp}$ and $\Delta_{sp}$, and increments in the contact forces are obtained by solving equation (A1). The increments in the contact forces are for the same contact combination produced by the linear solution and do not account for any change in the contact location. With this procedure, the increments to the contact forces obtained from the solution of equation (A1) may be positive, negative, or zero. This process is repeated until the increments for the contact forces are negligible compared with their total values.

## Appendix B

## Results for the Original SRM Joint Modified With Exterior Rings

When the motor cases are pressurized, the solid rocket motor (SRM) field joint develops substantial bending gradients near the O-rings, and these gradients are a result of the mismatch in the circumferential stiffness of the tang and clevis joint and the circumferential stiffness of the far-field shell wall. The O-ring gap changes depend to a great extent on the severity of these bending gradients. This observation suggests that placing one or more exterior rings of the correct proportions near a joint can shift the bending gradients away from the joint and thus reduce the size of the O-ring gap changes. (See figure 11.)

The results presented in figures 23 to 26 show the effects of ring location and ring thickness on the O-ring gap changes as a function of joint clearances for two SRM cases joined together by the original joint. The results presented in these figures correspond to the nominal 1000-psi pressure loading previously described and a pressure seal at the primary O-ring. The results shown in figures 23 to 26 correspond to clearances ranging from $\delta_1 = \delta_2 = 0$ to 0.050 in. and include combinations of clearances between these bounding values. Results for the original joint without rings are included in these figures for comparison with the results for the joint with rings.

The results presented in figure 23 are for two equally spaced (with respect to the centerline of the joint pin connection) rectangular D6AC steel rings that are nominally 4.50 in. wide by 0.50 in. thick in size. The ring locations investigated start at 6.00 in. from the centerline of the joint pin connection to the edge of the rings, and include locations up to 12.00 in. away from the pin. The ring location of 6.00 in. corresponds to the closest practical positioning of equally spaced rings next to the joint (because of the geometry of the clevis side of the joint). The results shown in figure 23 indicate that the O-ring gap changes decrease, and the sensitivity of the O-ring gap changes to the joint clearances somewhat diminishes, as the rings are placed closer to the joint. Moreover, the results indicate that the optimal ring location is between 6.00 and 7.00 in. from the pins. At this location, the rings reduce the O-ring gap changes by about 30 percent of the corresponding O-ring gap changes obtained for the SRM cases without rings.

The results presented in figure 24 show the effects on the O-ring gap changes of thickening the two equally spaced, 4.50-in.-wide rectangular rings attached to the SRM cases. The nearest edges of the rings are located 6.00 in. from the centerline of the pin connection. Figure 24 indicates that thickening the rings substantially reduces the O-ring gap changes (O-ring gap changes as small as 0.005 in.) and slightly reduces the sensitivity of the O-ring gap changes to the joint clearances. However, thickening the rings also causes an increase in the stresses in the shell wall adjacent to the rings. Results obtained from FASOR analyses indicate that significant increases in the stresses in the shell walls near the rings (up to values near the ultimate strength of the material) result from increasing the ring thickness to 2.00 in.

The results presented in figure 25 show the O-ring gap changes that result from placing a single ring on the tang side of the joint. The ring is nominally 4.50 in. wide by 0.50 in. thick. The ring is placed on the tang side of the joint to augment the lower circumferential stiffnesses of the tang and thus reduce the mismatch in circumferential stiffness between the tang and clevis. The ring locations investigated start at 3.00 in. from the centerline of the joint pin connection to the edge of the ring and include locations up to 15.00 in. away from the pin centerline. The ring location of 3.00 in. corresponds to the closest practical positioning of a single ring on the tang side of the joint. The results shown in figure 25 indicate that placing a single ring on the tang side of the joint results in only slight reductions in the O-ring gap changes. The O-ring gap changes are about 20 percent less than the O-ring gap changes for the same joint without a ring for a ring location of approximately 5 in. from the centerline of the pin.

The results presented in figure 26 show the effects on the O-ring gap changes of thickening the rectangular ring attached to the SRM case. The nearest edge of the ring is located 6.55 in. from the centerline of the pin connection. Unlike the results obtained for two rings placed on the SRM cases (see fig. 24), the results presented in figure 26 indicate that thickening the one ring results in only slight reductions in the O-ring gap changes and results in essentially no reduction in the sensitivity of the O-ring gap changes to joint clearances. Moreover, thickening the ring also causes significant increases in the stresses in the shell wall adjacent to the ring, and these stresses may lead to substantial inelastic deformation of the SRM case.

The results presented in figures 23 and 24 indicate that placing two rings on the SRM cases reduces the O-ring gap changes, particularly as the rings are made thicker. However, restricting an appropriate design to be one in which the stresses in the shell wall are substantially below the yield stress of the

material mandates the use of relatively thin rings. It is important to eliminate these high stresses in the joint and shell wall to allow the reuse of the boosters. In addition, the results of figures 23 to 26 indicate that placing one ring instead of two rings on the SRM case is not as effective in reducing the O-ring gap changes or in reducing their sensitivity to joint clearances. Comparing the results of figures 23 to 26 with the results shown in figures 14 to 16 for the redesigned joint (and the relative size of the stresses in the shell wall due to the rings) suggests that the redesigned joint is a much more effective means of reducing the O-ring gap changes. In addition, the redesigned joint is much less sensitive to joint clearances than the original joint combined with either one or two rings on the SRM cases.

## Appendix C

## Results for the Eccentric- and Kinked-Shell-Wall Modifications

### Eccentric-Shell-Wall Modification

One way of reducing the O-ring gap changes of the original joint is to build a slight eccentricity into the nearby shell wall. As the SRM pressurizes and stretches axially, the eccentric load path acts to reduce the O-ring gap changes. The eccentricity is built into the structure by machining the tang and the clevis into the SRM cases such that their radial distance from the center of the case is less than the radial distance of the adjoining shell wall. (See fig. 11.) More precisely, the eccentricity used herein is defined as the radial distance from the midsurface of the uniform far-field shell wall to the reference surface of the tang defined in figure 3(a). The amount of the eccentricity investigated in this paper is on the order of the shell wall thickness (0.4790 in.).

The results presented in figures 27 to 32 show the effects on the O-ring gap changes of joining two SRM cases with an eccentric tang and clevis joint. The results presented in these figures are for a nominal internal pressure loading of 1000 psi acting on the joint with a pressure seal at the primary O-ring. Additional results are also presented for a compression loading equal in magnitude to the induced axial tension loading associated with the nominal pressure loading. The band of results shown in figures 27 to 32 corresponds to joints with clearances ranging from $\delta_1 = \delta_2 = 0$ to 0.050 in. and includes all combinations of clearances in between these bounding values.

Results showing the effects of eccentricity $e$ on the O-ring gap changes are presented in figure 27. An additional parameter appearing in this figure is the length of the shell wall taper that is used to connect the eccentric joint to the SRM cases. Results for the original joint design are also presented in figure 27 for comparison with those of the eccentric joint design. The shell wall taper starts 3.80 in. from the centerline on both sides of the joint pin connection and extends axially for length $l$. Results are presented in this figure for $l = 1.10$ and 2.20 in. Figure 27 indicates that as the eccentricity increases the O-ring gap changes decrease substantially and the sensitivity of the O-ring gap changes to joint clearances also decreases somewhat. Moreover, this figures shows that $l = 1.10$ in. is more effective in reducing the O-ring gap changes than $l = 2.20$ in. When $l = 1.10$ in., the O-ring gap changes can be eliminated altogether with an eccentricity of about one shell wall thickness. When $l = 2.20$ in., the O-ring gap changes can be eliminated altogether with an eccentricity of about two shell wall thicknesses.

Figure 28 shows the effects on the O-ring gap changes of varying the axial location of shell wall taper ($l = 1.10$ in.) with $e = 1.00$ in. Results for the original SRM joint design are also presented in figure 28 for comparison with those of the eccentric joint design. These results indicate that the O-ring gap changes are zero for taper locations less than about 4.50 in. from the centerline of the joint pin connection. As the taper location moves away from the pin both the O-ring gap changes and their sensitivity to joint clearances increase substantially. At locations greater than about 6 in. from the pin the O-ring gap changes of the eccentric joint exceed the O-ring gap changes of the original joint. The O-ring gap changes begin to slightly decrease for taper locations greater than about 8 in. The maximum O-ring gap changes are about 0.04 in. for a taper location about 8 in. from the pin. This reduction is attributed to the oscillatory nature of the bending moment induced in the shell by the eccentric load path.

Prior to ignition, the SRB's experience compression loads because of the weight of the vehicle and because of the Space Shuttle main engine operation. A potentially adverse effect of shell wall eccentricity is to cause large O-ring gap changes or cause bending moments that may overstress the joints during prelaunch compression loadings. Large O-ring gap changes associated with a compression loading may permit slippage or misplacement of the O-rings prior to motor pressurization, either of which could result in loss of joint pressure seal and vehicle failure.

To determine the sensitivity of the O-ring gap changes to compression loading, results for a compression loading equal in magnitude to the axial load induced by motor pressurization (i.e., 36 345 lb/in. without internal pressure) were obtained. These results and the results from figure 27 are presented together in figure 29 for comparison. The results presented in figure 29 are for $l = 1.10$ in. and $\tilde{d} = 3.80$ in. Figure 29 shows that the O-ring gap changes increase with increasing eccentricity and are considerably more sensitive to joint clearances when the shell is subjected to the compression loading. Figure 29 also indicates that joints having an eccentricity of about 0.40 in. exhibit O-ring gap changes of about 0.006 in. for both types of loading.

The results presented in figures 27 to 29 suggest that the eccentric-shell-wall concept can be used to reduce O-ring gap changes. However, results obtained from FASOR analyses also indicate that stresses on the order of the yield stress of the material are present in the shell wall near the taper.

The analyses also indicate that as the shell wall eccentricity increases, so do the stresses. These results were obtained for joints with $e = 0.25$ and 1.00 in. and $l = 1.10$ in. The results specifically indicate that increasing the eccentricity from 0.25 to 1.00 in. increases the stresses in the shell wall near the taper from values near the yield stress of the material to values nearly double the ultimate strength of the material.

The results presented in figures 30 and 31 indicate the importance of geometric nonlinearity on the O-ring gap changes as a function of joint clearances and internal pressure for joints with $e = 0.25$ and 0.74 in. Figure 30 indicates a slight increase in O-ring gap changes and a slight reduction in their sensitivity to joint clearances when geometric nonlinearity is included in the analysis. Comparing the results presented in figures 30 and 31 indicates increasing differences between the O-ring gap changes obtained from linear and nonlinear analyses as the shell wall eccentricity increases. The sensitivity of the O-ring gap changes to joint clearances appears to be about the same for results presented in figure 31 ($e = 0.74$ in.).

The results presented in figure 32 indicate the importance of geometric nonlinearity on the O-ring gap changes as a function of joint clearances and axial load ratio for joints with $e = 0.74$ in. The results presented in this figure are for the compression loading previously discussed. Figure 32 indicates that geometric nonlinearity is important in the analysis of the compression loaded joint. Including geometric nonlinearity in the FASOR analyses results in O-ring gap changes that are approximately twice the corresponding O-ring gap changes obtained from linear analyses. The sensitivity of the O-ring gap changes to joint clearances appears to be about the same in each case.

The results presented in figures 27 to 32 suggest that the eccentric-shell-wall concept is an effective means of controlling the O-ring gap changes. However, because of the high stresses associated with the eccentricity, the eccentric joint concept is not an attractive SRM joint design modification. Moreover, the O-ring gap changes and sensitivity to geometric nonlinearity associated with compression loadings also detract from the attractiveness of this joint concept as an SRM joint modification.

### Kinked-Shell-Wall Modification

The idea behind the kinked-shell-wall modification depicted in figure 11 is to introduce a local bending moment that acts to reduce the O-ring gap changes when the SRB is pressurized. Shell wall kinks 1.10 in. long and located 3.80 in. from the centerline on both sides of the joint pin connection were used to investigate this concept. Results of FASOR analyses indicate that the shell wall kinks are effective in reducing the O-ring gap changes but produce extremely high stresses in the kinked-shell-wall region. As a result of these high stresses, the kinked-shell-wall concept is not an attractive SRM joint modification.

## References


1. Presidential Commission on the Space Shuttle Challenger Accident: *Report of the Presidential Commission on the Space Shuttle Challenger Accident, Volumes I–V.* June 6, 1986.
2. Nemeth, Michael P.; and Anderson, Melvin S.: Axisymmetric Shell Analysis of the Space Shuttle Solid Rocket Booster Field Joint. *J. Spacecr. & Rockets,* vol. 27, no. 1, Jan.–Feb. 1990, pp. 85–92.
3. Greene, William H.; Knight, Norman F., Jr.; and Stockwell, Alan E.: Structural Behavior of the Space Shuttle SRM Tang-Clevis Joint. *J. Propuls. & Power,* vol. 4, no. 4, July–Aug. 1988, pp. 317–327.
4. Card, Michael F.; and Wingate, Robert T.: Structural Behavior of Solid Rocket Motor Field Joints. AIAA-87-0701, Apr. 1987.
5. Hill, M. L.; Coulter, J. C.; Matharu, S. S.; and Whelchel, T. M.: *Solid Rocket Motor—Critical Design Review (CDR) Structural Analysis of the Solid Rocket Motor Redesigned Field Joint.* MSFC-RPT-1474, NASA George C. Marshall Space Flight Center, 1987.
6. *User Manual for SRA/FASOR—A Program for Stress, Buckling, and Vibration Analysis of Elastic-Plastic or Anisotropic Shells of Revolution Based on Classical or Transverse Shear Deformation Theories.* Structures Research Assoc., c.1989.
7. Oostyen, J. E.; Bright, D. D.; Hawkins, G. F.; McCluskey, P. M.; and Larsen, G. L.: *SRM Joint Deflection Referee Test: Phase 2 Final Report.* Doc. TWR-300149, Morton-Thiokol Inc., Wasatch Operations, Apr. 1986.

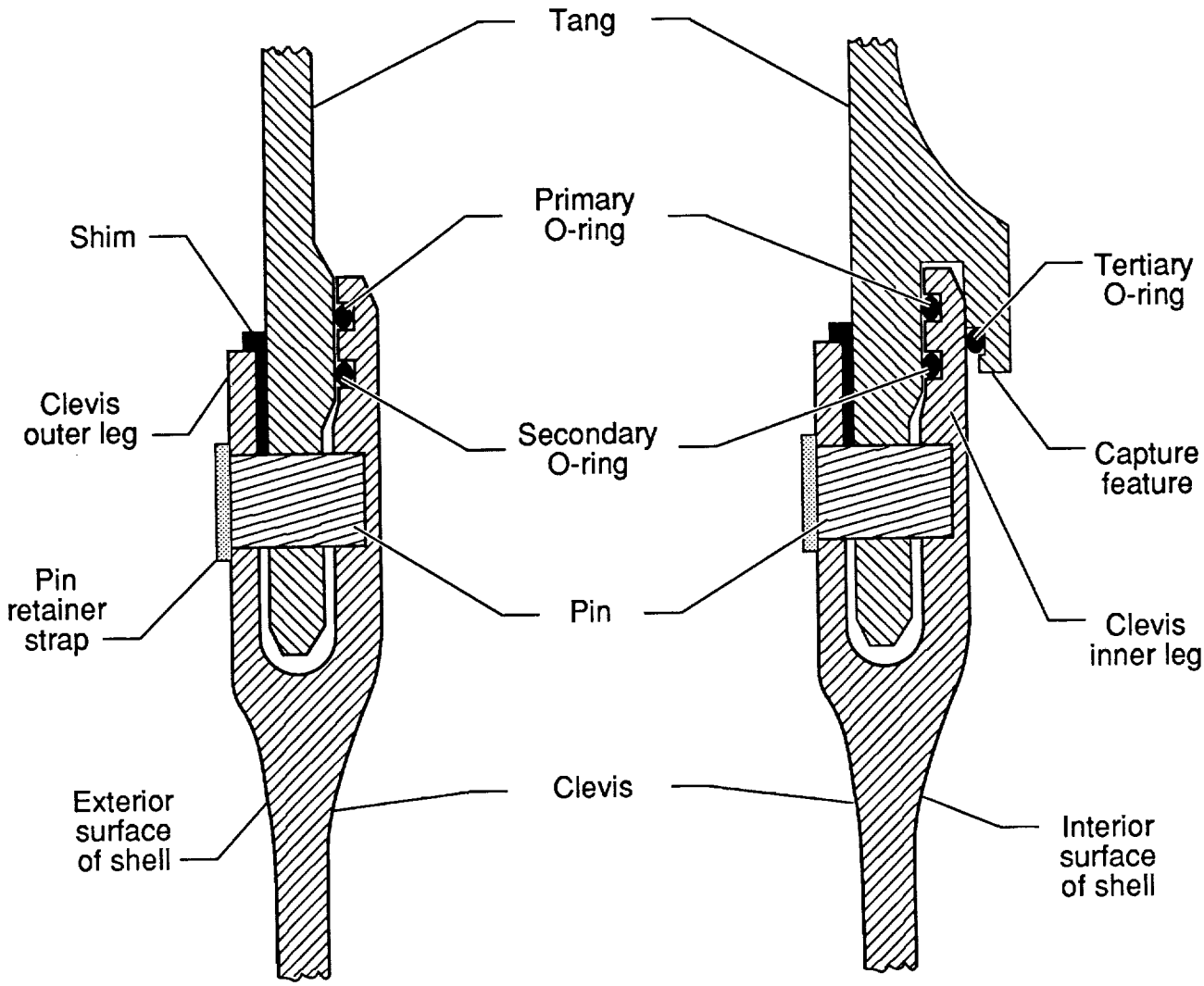


(a) Original joint.

(b) Redesigned joint.

Figure 1. Cross sections of original and redesigned SRB field joints.

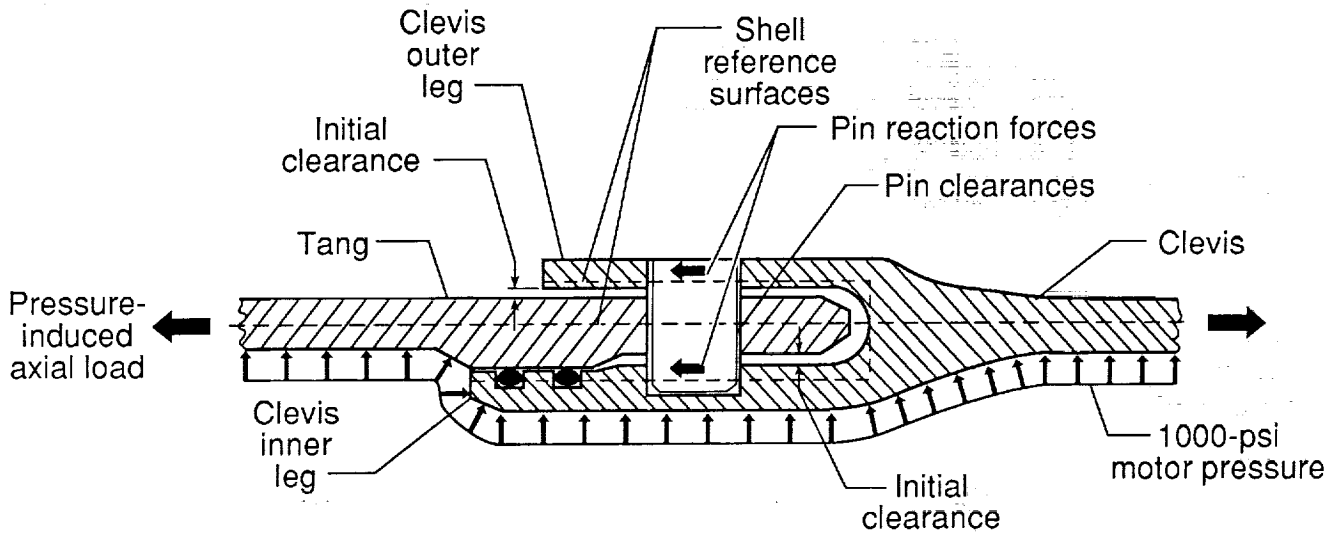


Figure 2. Characteristics of original joint.

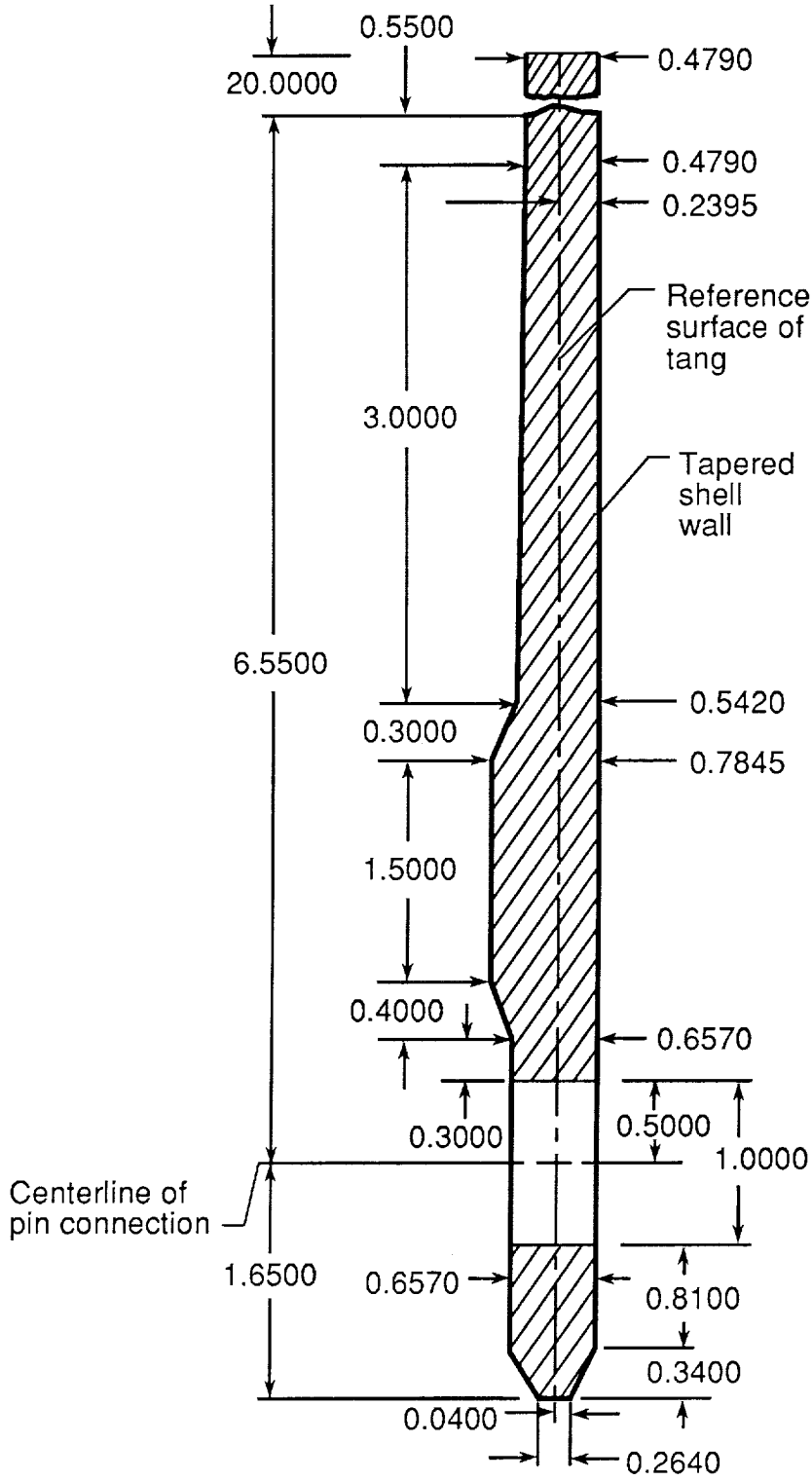


(a) Original-joint tang dimensions.

Figure 3. Dimensions of original and redesigned joints. (Not to scale; all dimensions in inches.)

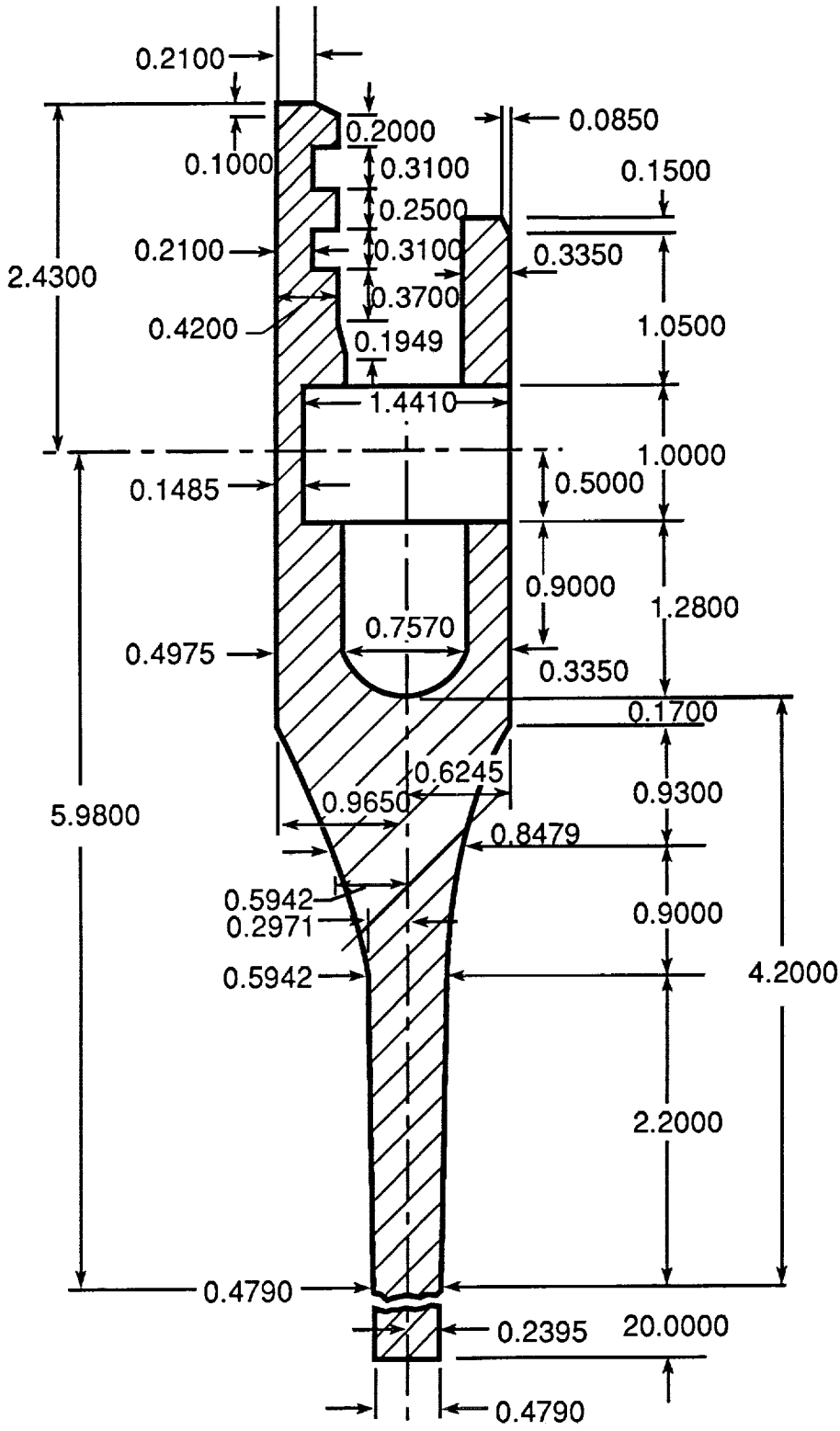


(b) Original-joint clevis dimensions.

Figure 3. Continued.

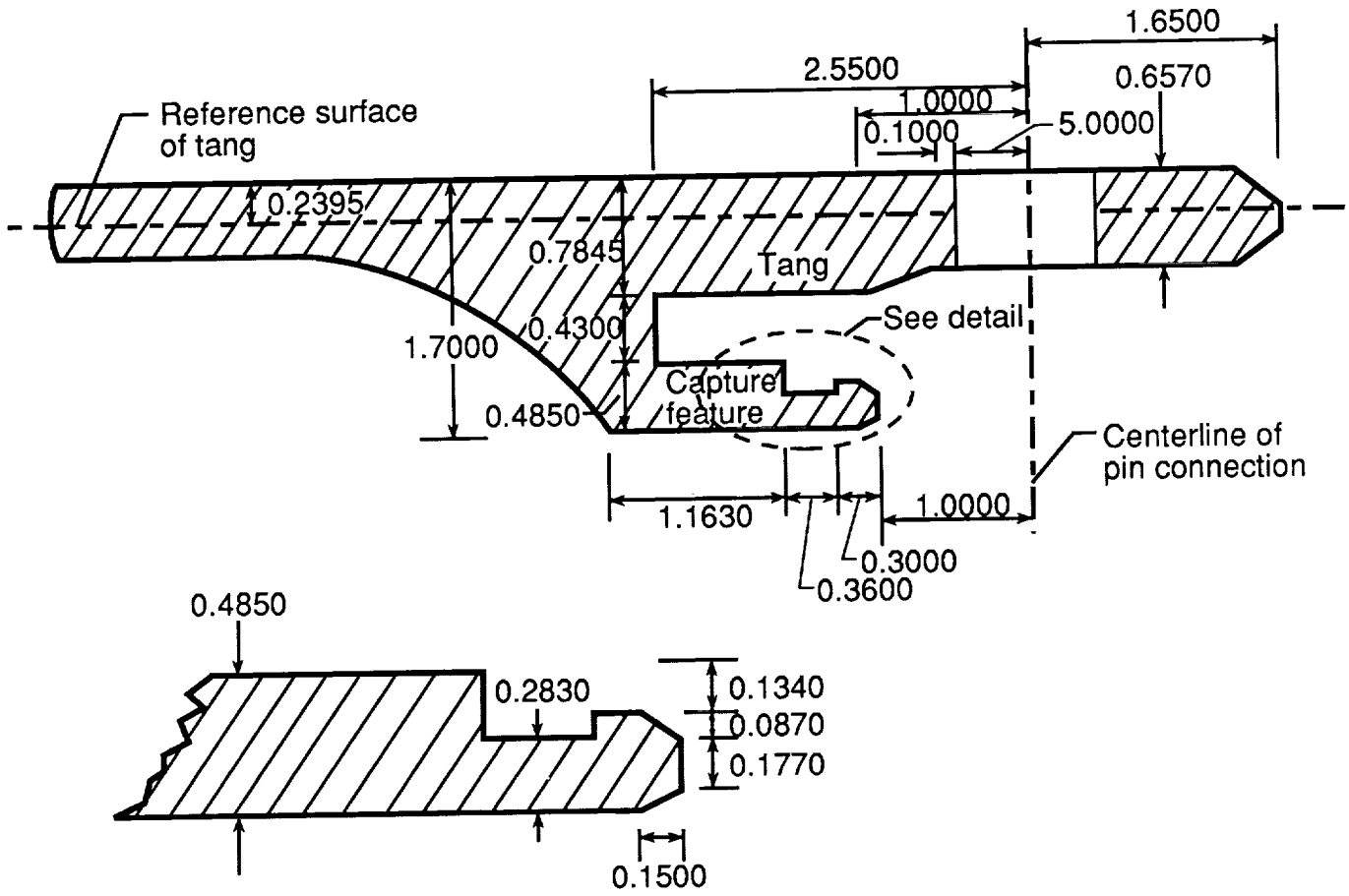


(c) Redesigned-joint tang and capture feature dimensions.

Figure 3. Continued.

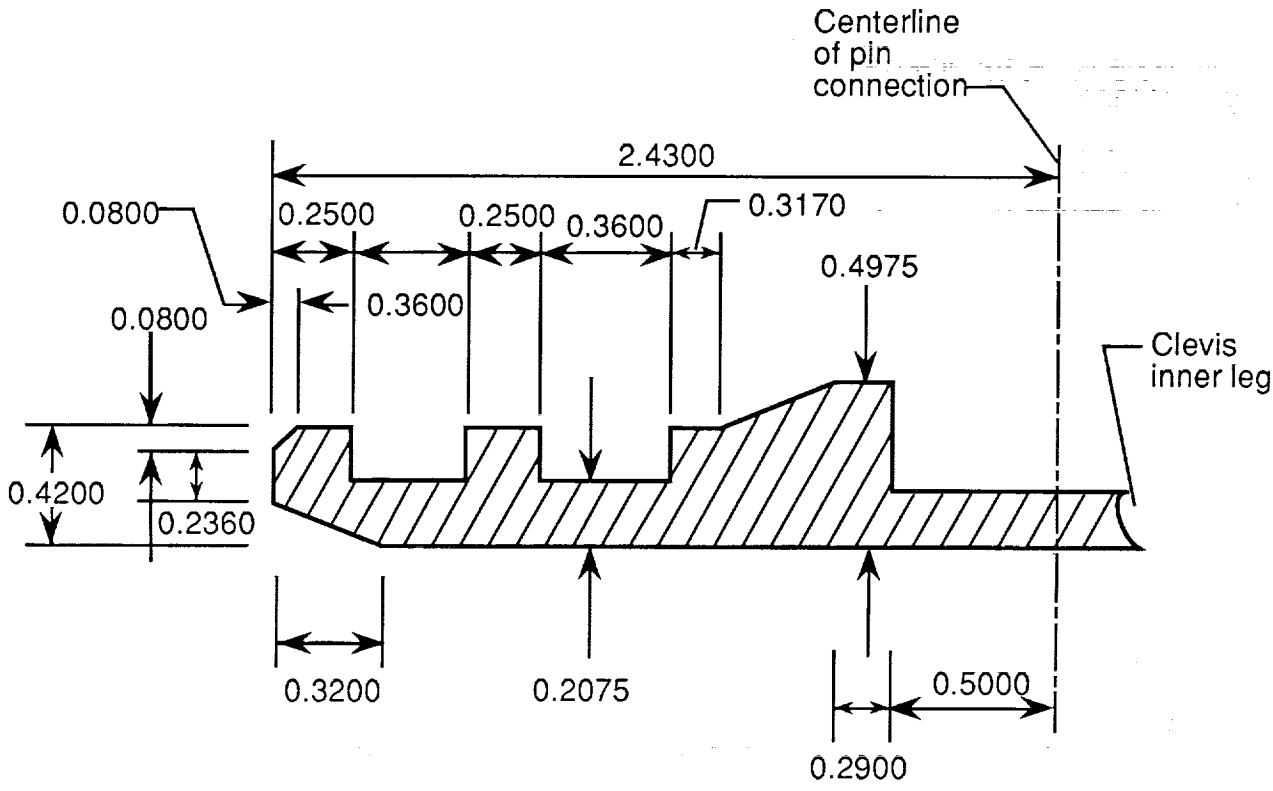


(d) Redesigned-joint clevis inner leg dimensions.

Figure 3. Concluded.

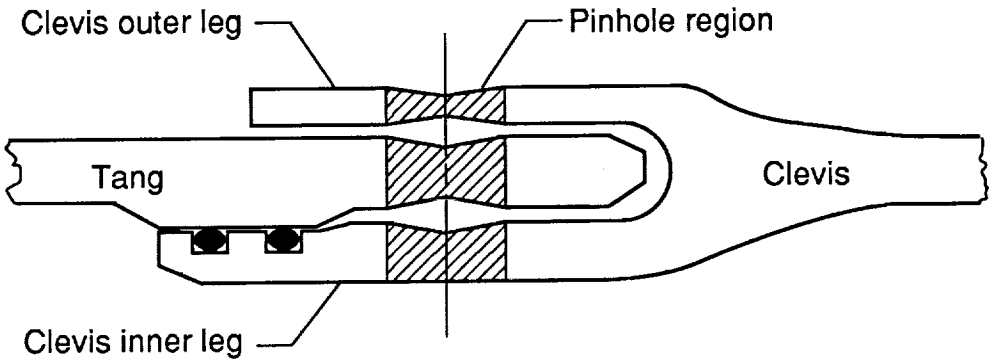


(a) Pinhole region of linear thickness variation.

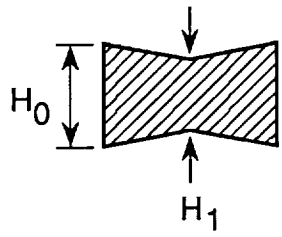


(b) Linear thickness variation for tang or clevis pinhole regions.

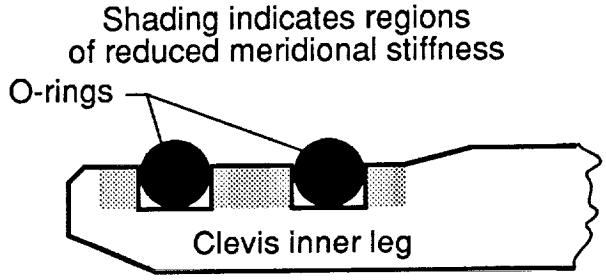


(c) O-ring groove detail.

Figure 4. Pinhole and O-ring groove modeling details for original joint.

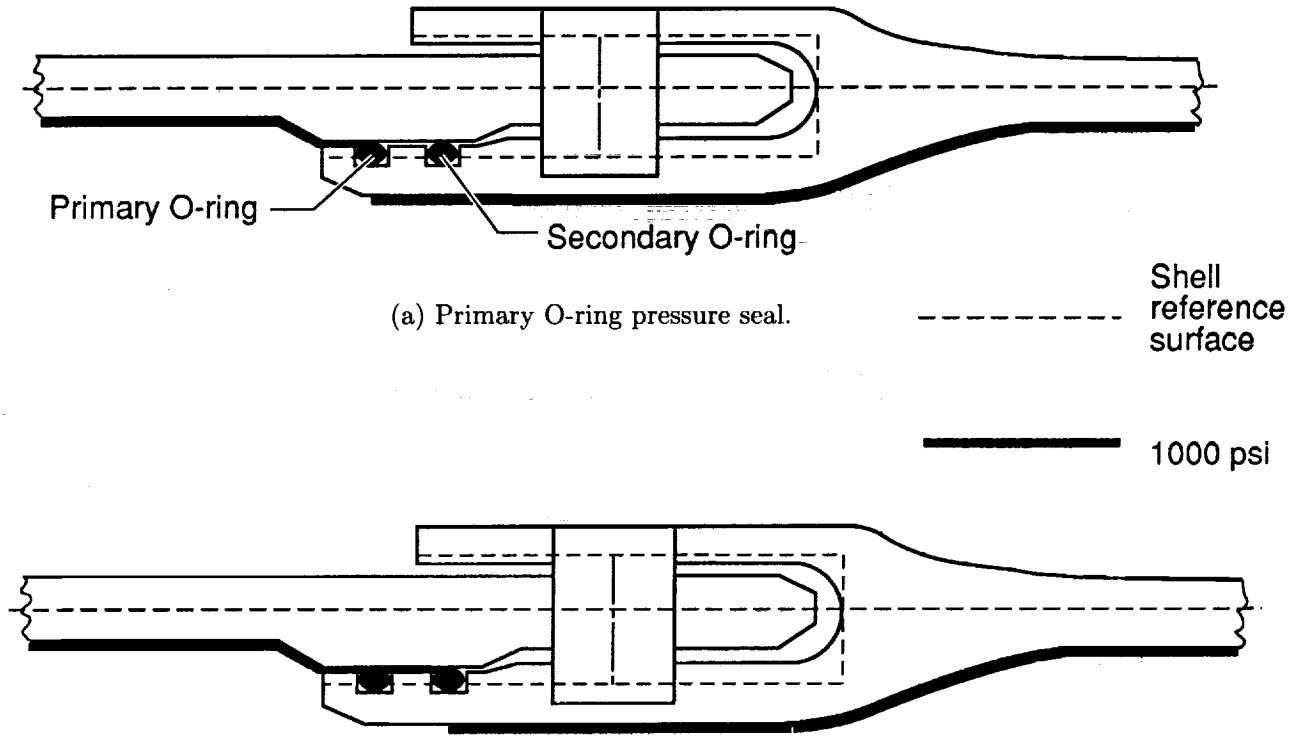


(a) Primary O-ring pressure seal.

(b) Secondary O-ring pressure seal.

Figure 5. Pressure distributions for original joint. (Bold line denotes regions where normal pressure of 1000 psi acts.)

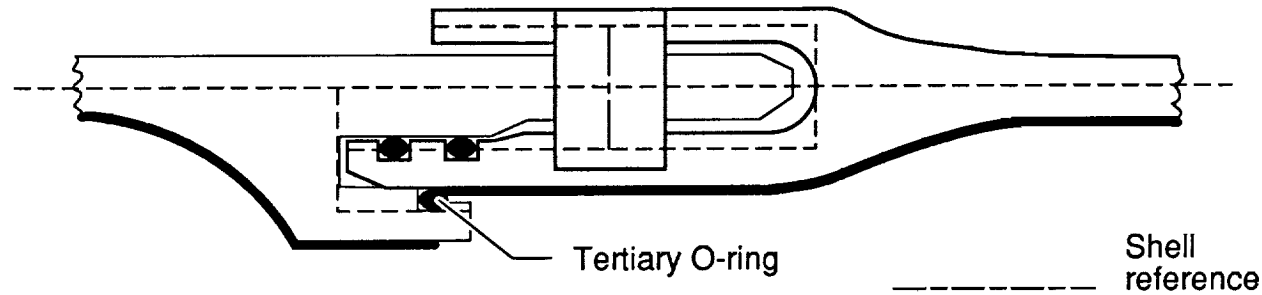


(a) Tertiary O-ring pressure seal.

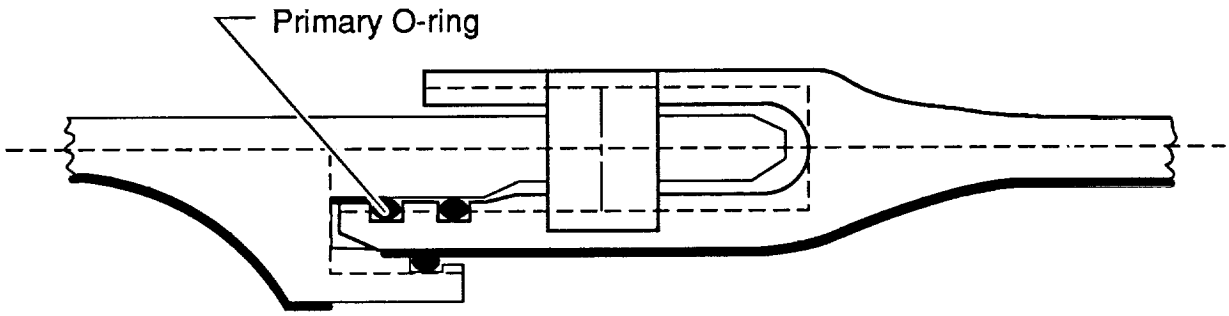


(b) Primary O-ring pressure seal.

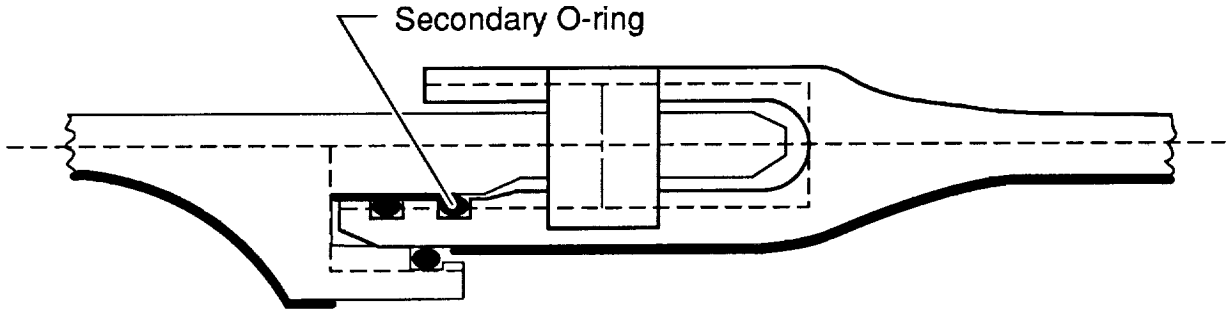


(c) Secondary O-ring pressure seal.

Figure 6. Pressure distributions for redesigned joint. (Bold line denotes regions where normal pressure of 1000 psi acts.)

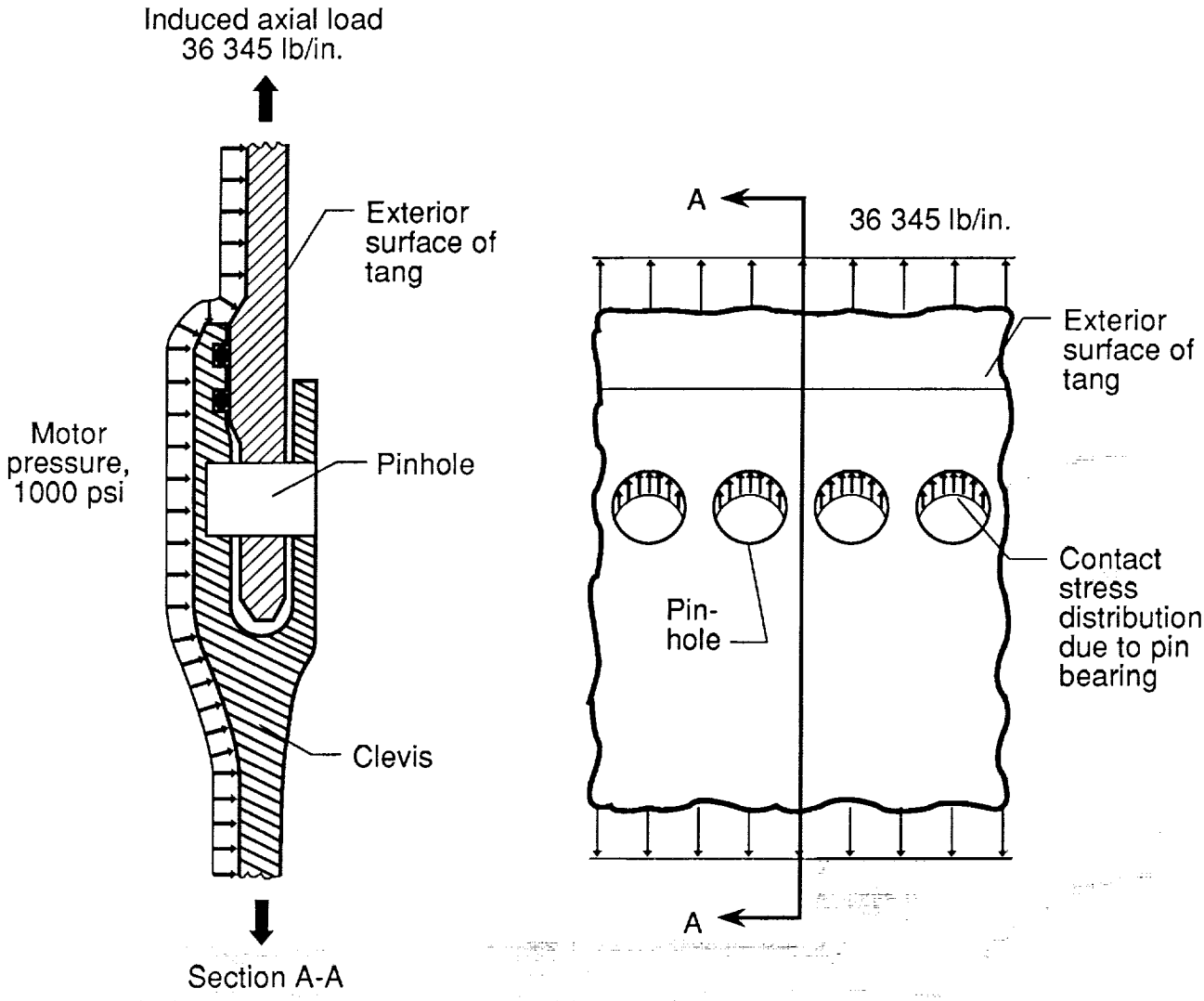


Figure 7. Pin bearing stress distribution for original joint.

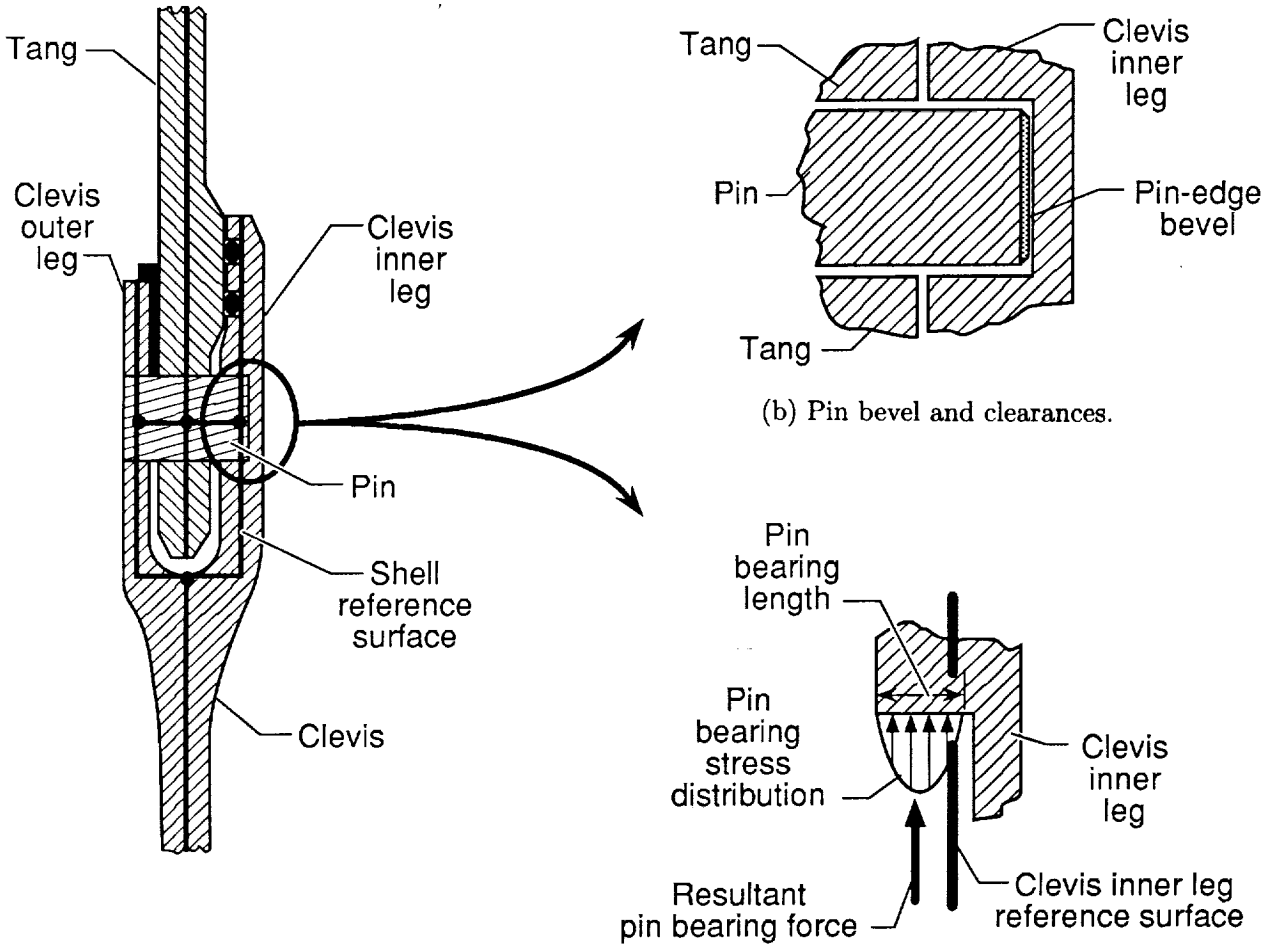


(a) Original joint.

(b) Pin bevel and clearances.

(c) Pin bearing details.

Figure 8. Details of pin bearing through-the-thickness stress distribution.

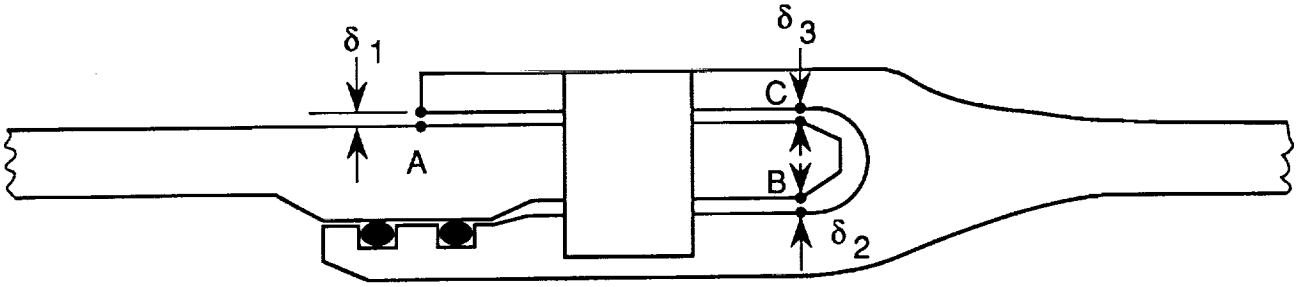


(a) Original joint.

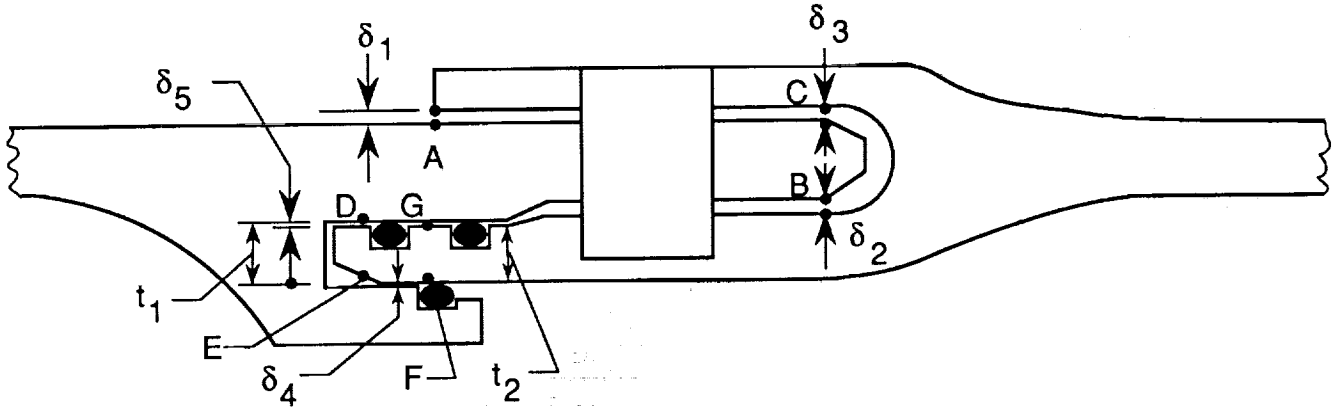


(b) Redesigned joint.

Figure 9. Clearances and contact points for original and redesigned field joints.

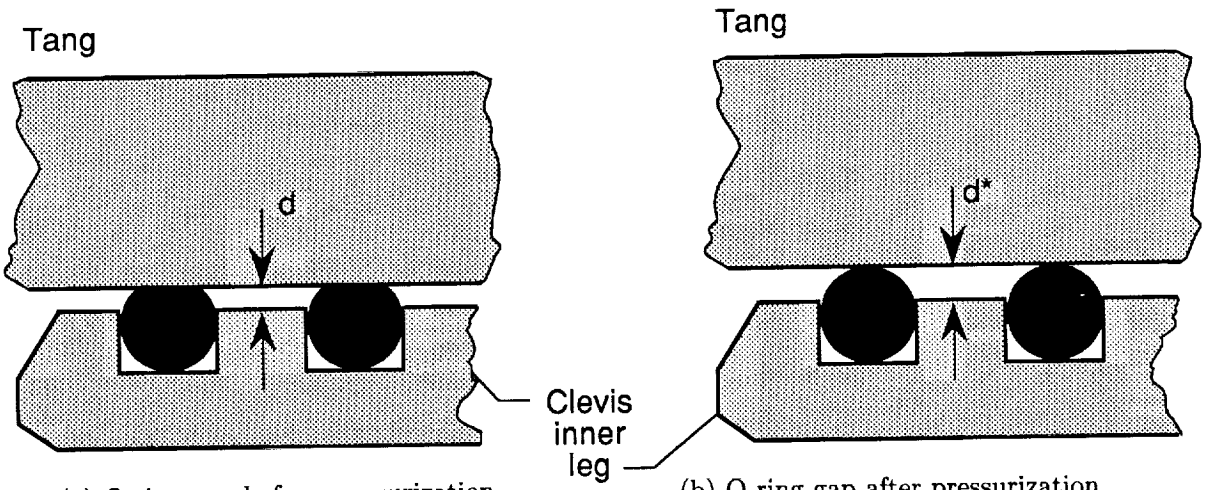


(a) O-ring gap before pressurization.

(b) O-ring gap after pressurization.

Figure 10. Gap change $\Delta = d^* - d$ at O-rings.

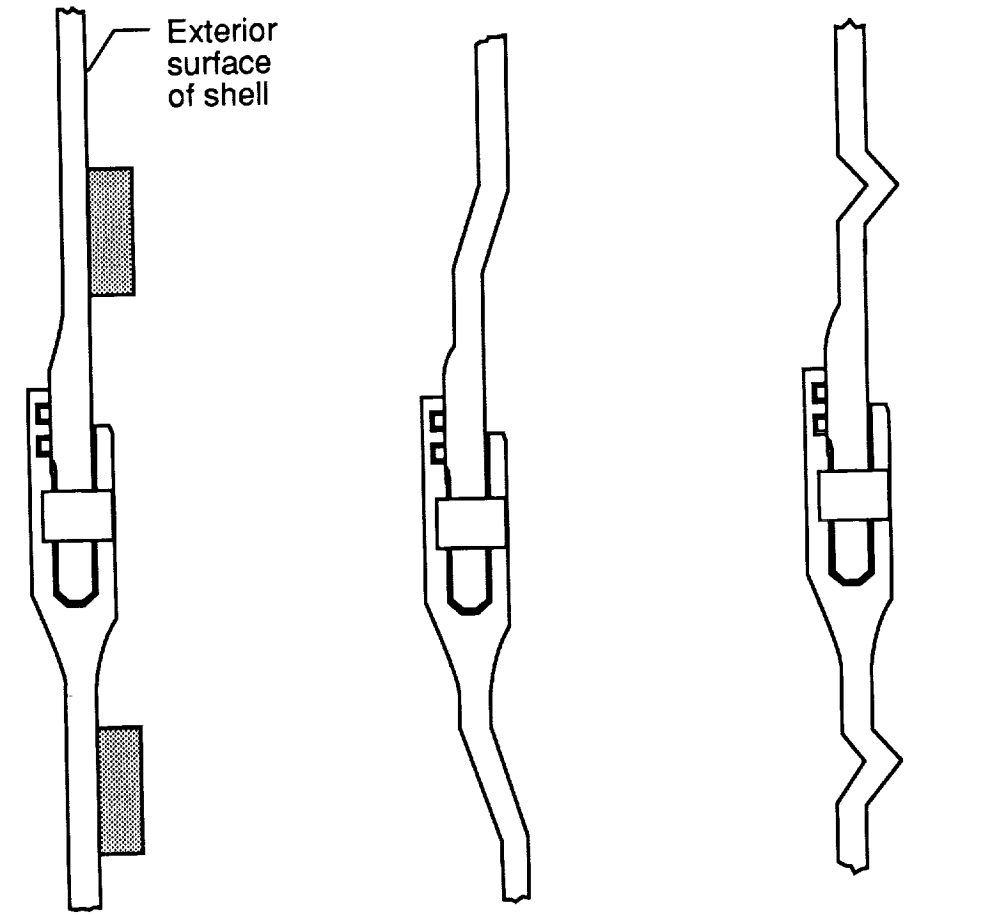


(a) Exterior ring modification.

(b) Eccentric-shell-wall modification.

(c) Kinked-shell-wall modification.

Figure 11. Joint design modifications.

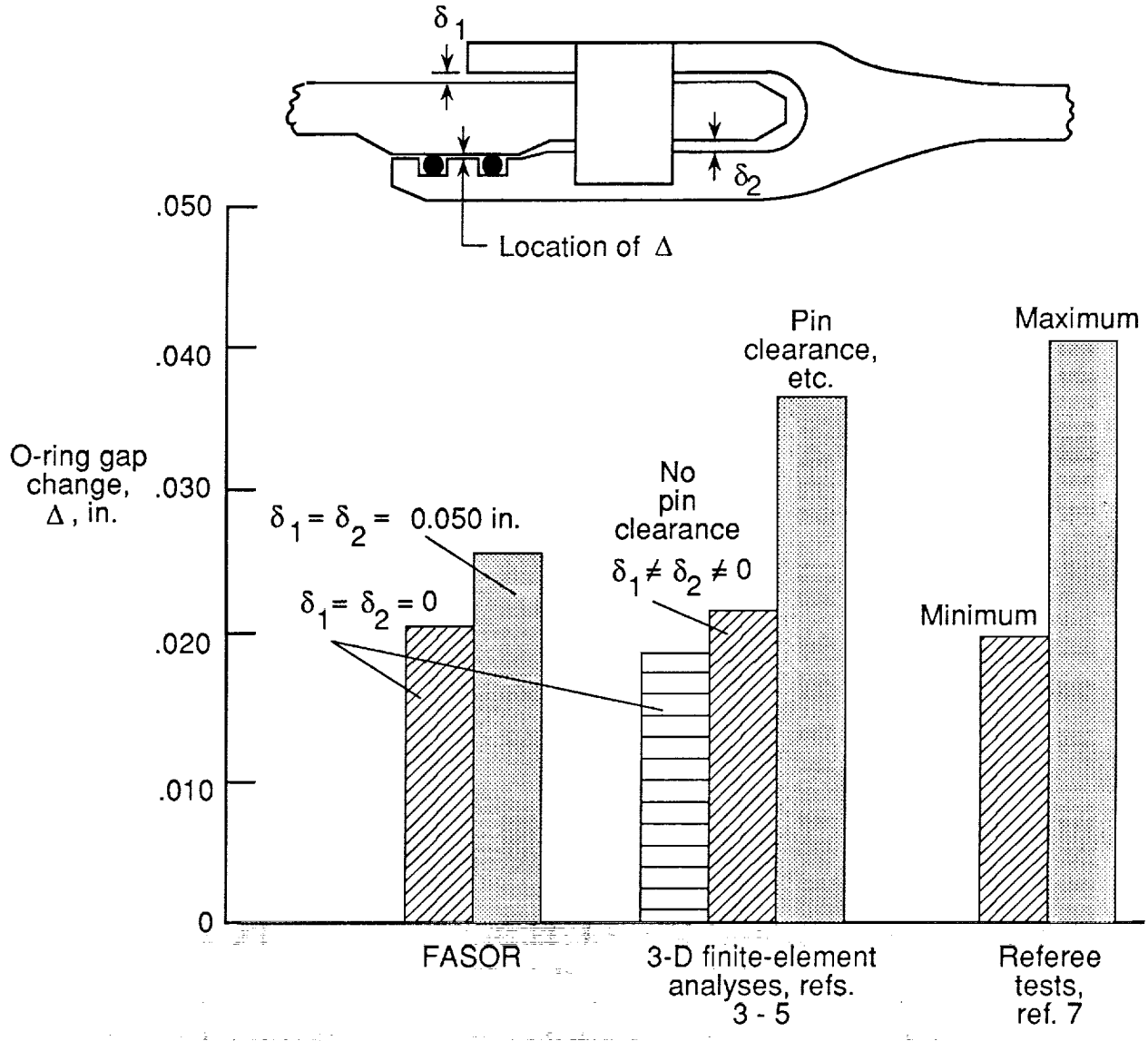


Figure 12. O-ring gap changes obtained from 2-D and 3-D analyses and experimental results for original joint.

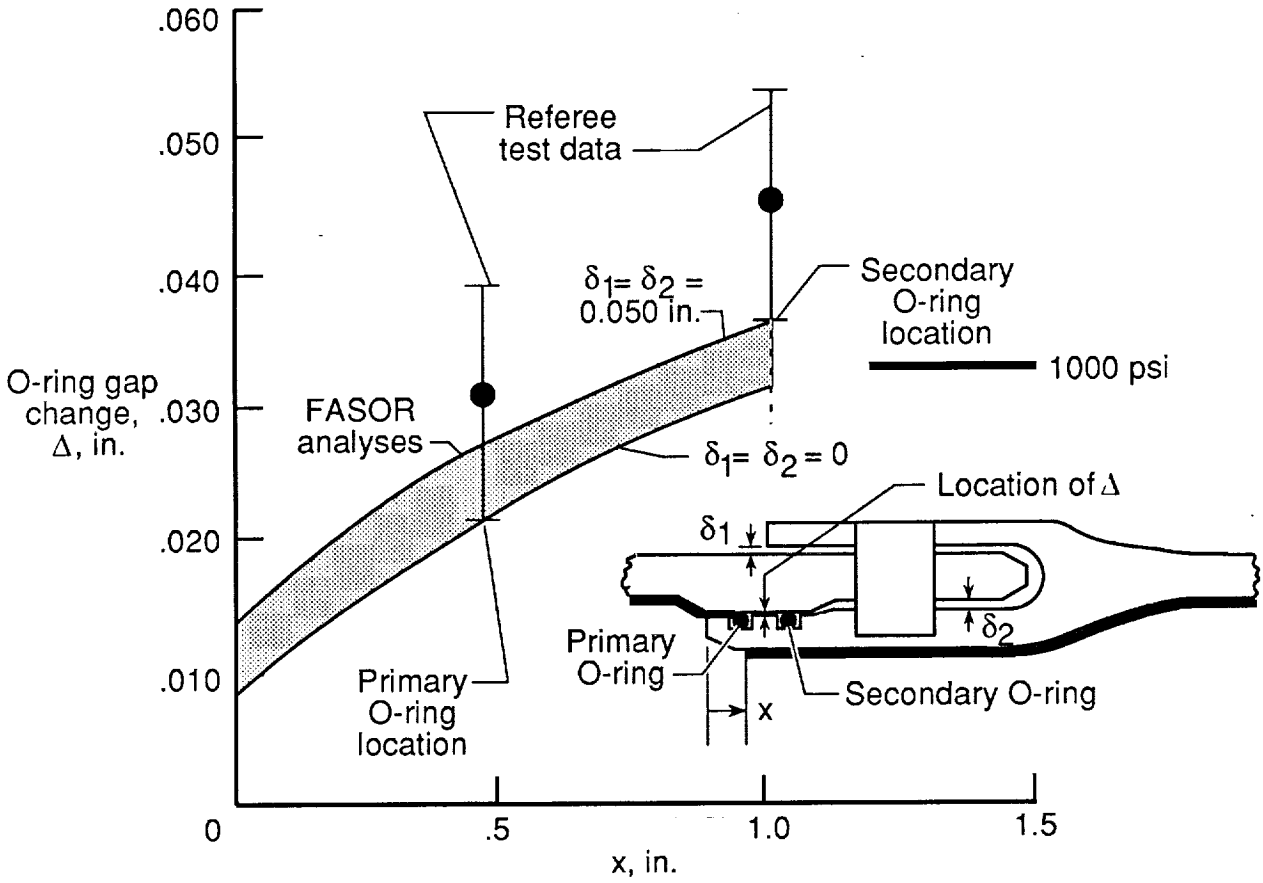


Figure 13. Effects of pressure seal location on O-ring gap changes for original joint. (Bold line denotes regions where 1000-psi normal pressure acts.)

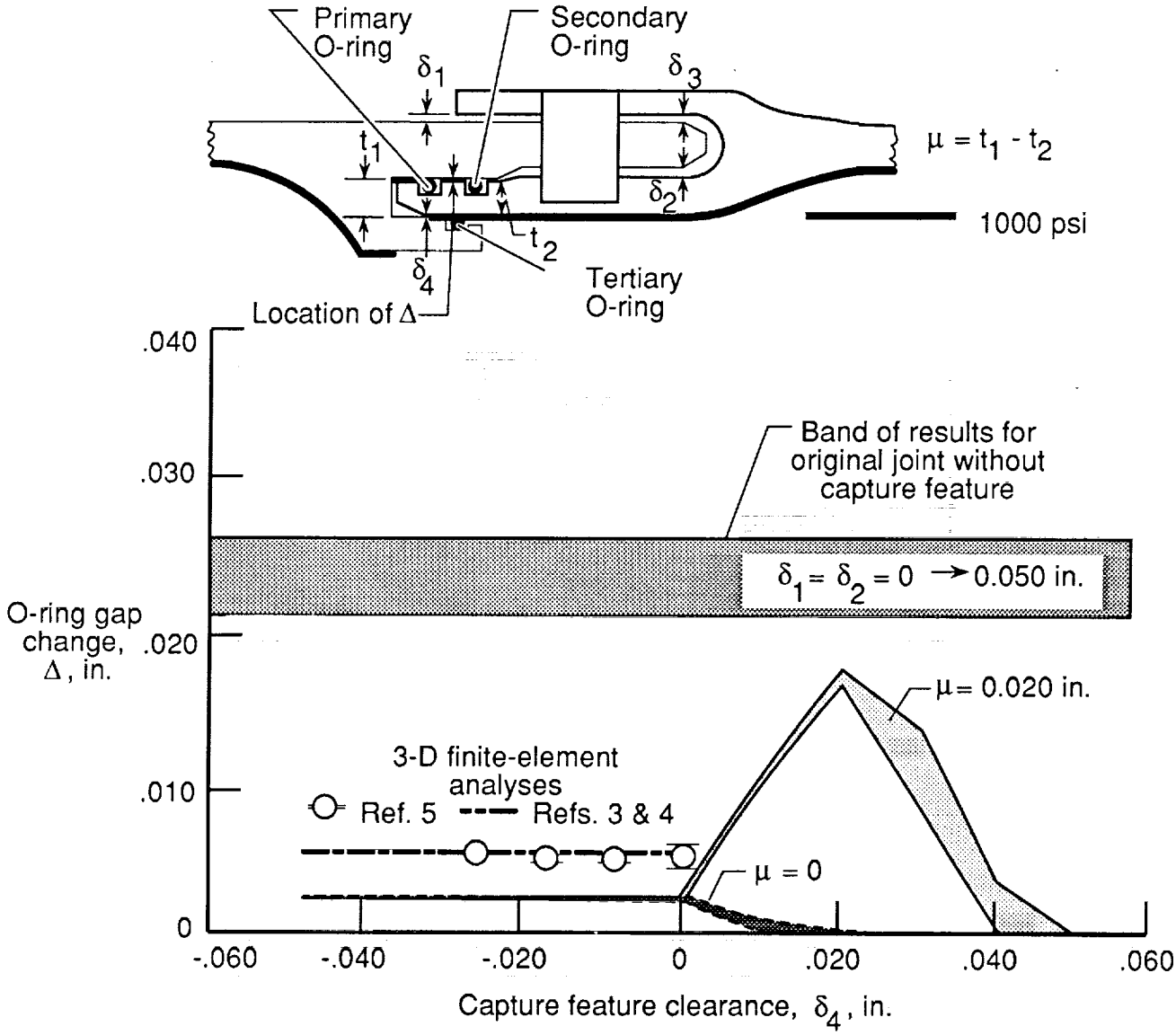


Figure 14. Effects of clearances on O-ring gap changes for redesigned joint with pressure seal at primary O-ring. (Bold line denotes regions where 1000-psi normal pressure acts; band of results for $\delta_1 = \delta_2 = 0$ to 0.050 in.)

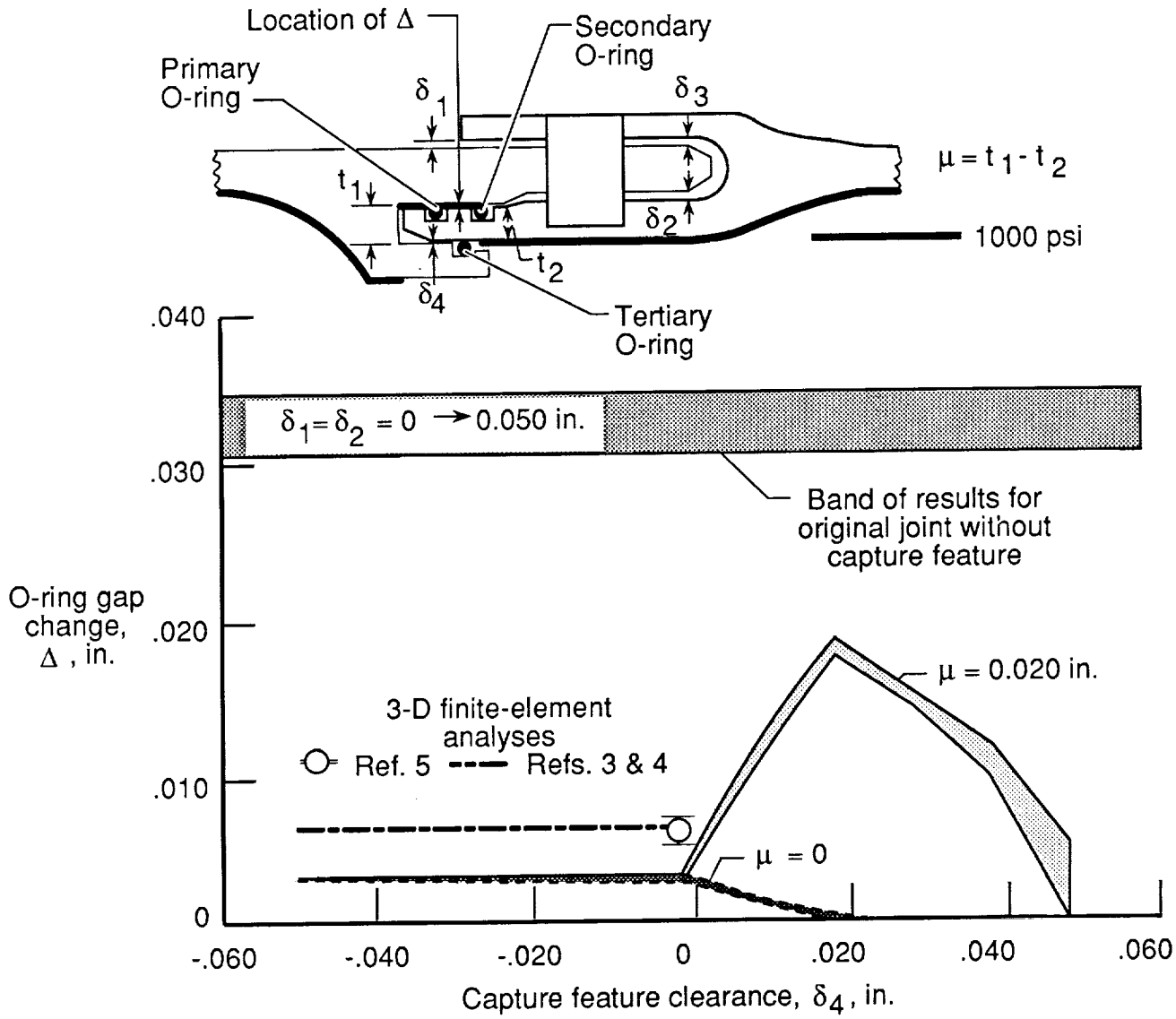


Figure 15. Effects of clearances on O-ring gap changes for redesigned joint with pressure seal at secondary O-ring. (Bold line denotes regions where 1000-psi normal pressure acts; band of results for $\delta_1 = \delta_2 = 0$ to 0.050 in.)

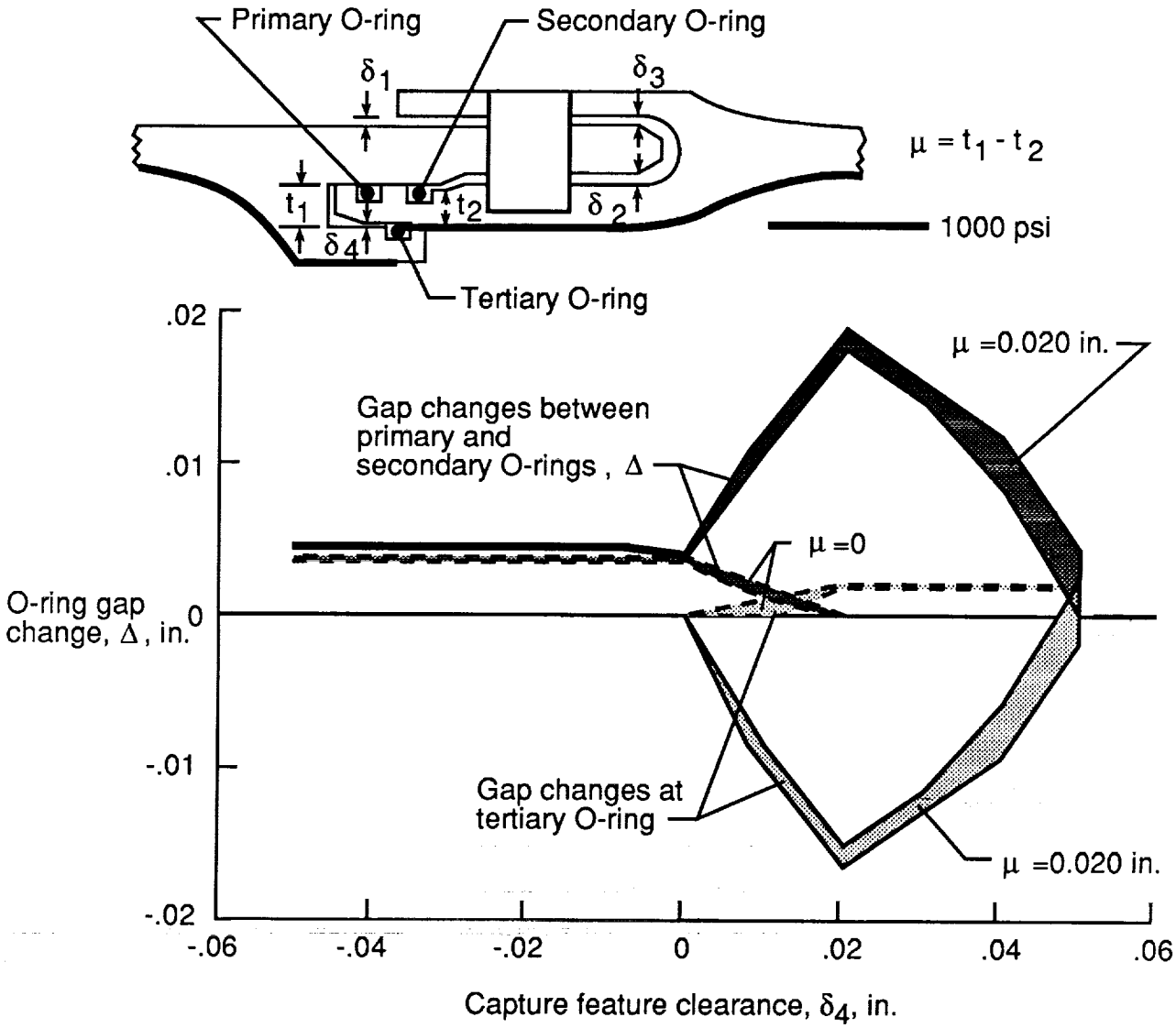


Figure 16. Effects of clearances on O-ring gap changes and gap change at tertiary O-ring of redesigned joint with pressure seal at tertiary O-ring. (Bold line denotes regions where 1000-psi normal pressure acts; band of results for $\delta_1 = \delta_2 = 0 \rightarrow 0.050$ in.)

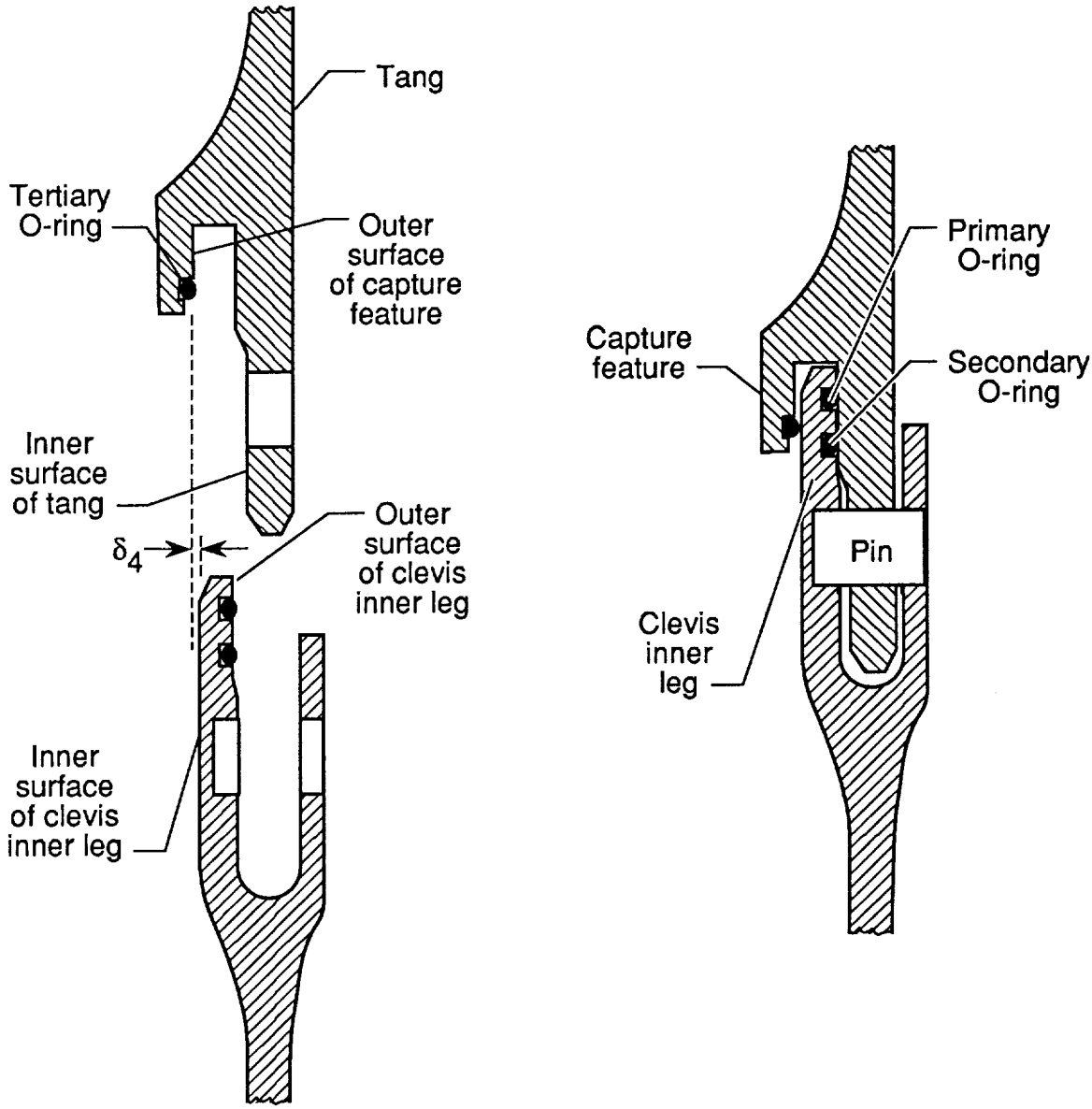


(a) Prior to assembly.

(b) Assembled and unpressurized.

Figure 17. Capture feature clearances of redesigned field joint for $\delta_4 > 0$.

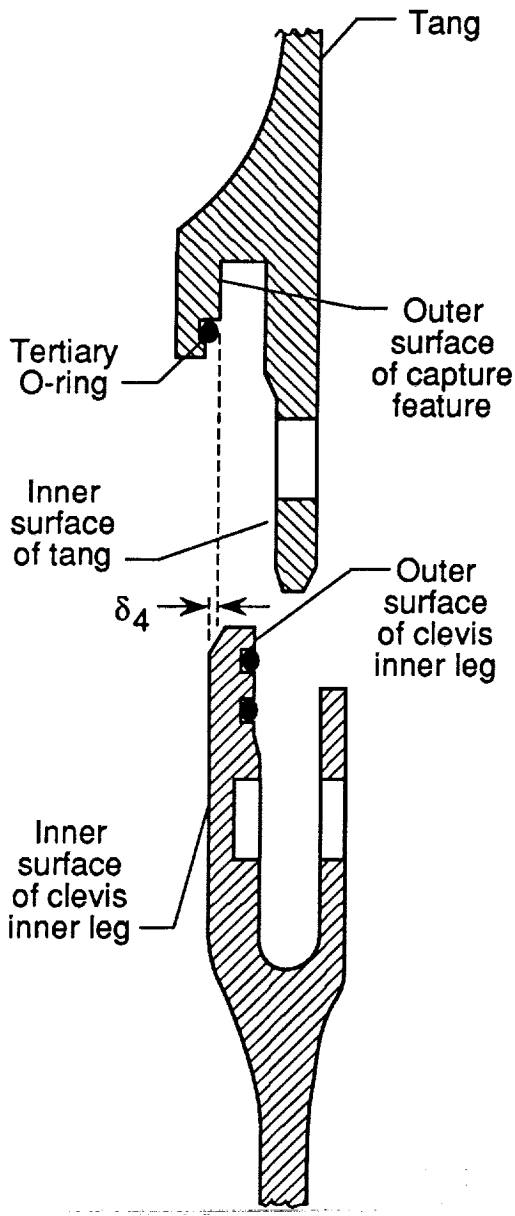


(a) Prior to assembly.

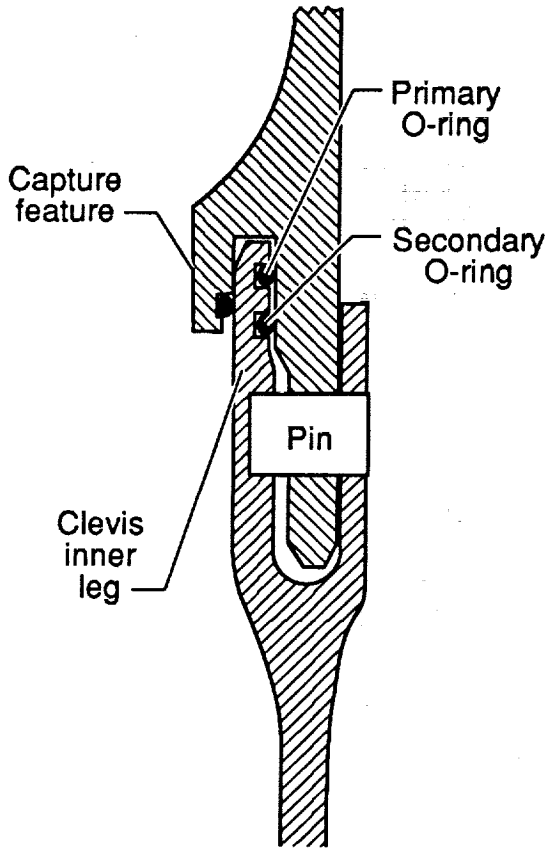


(b) Assembled and unpressurized.

Figure 18. Capture feature clearances of redesigned field joint for $\delta_4 < 0$.

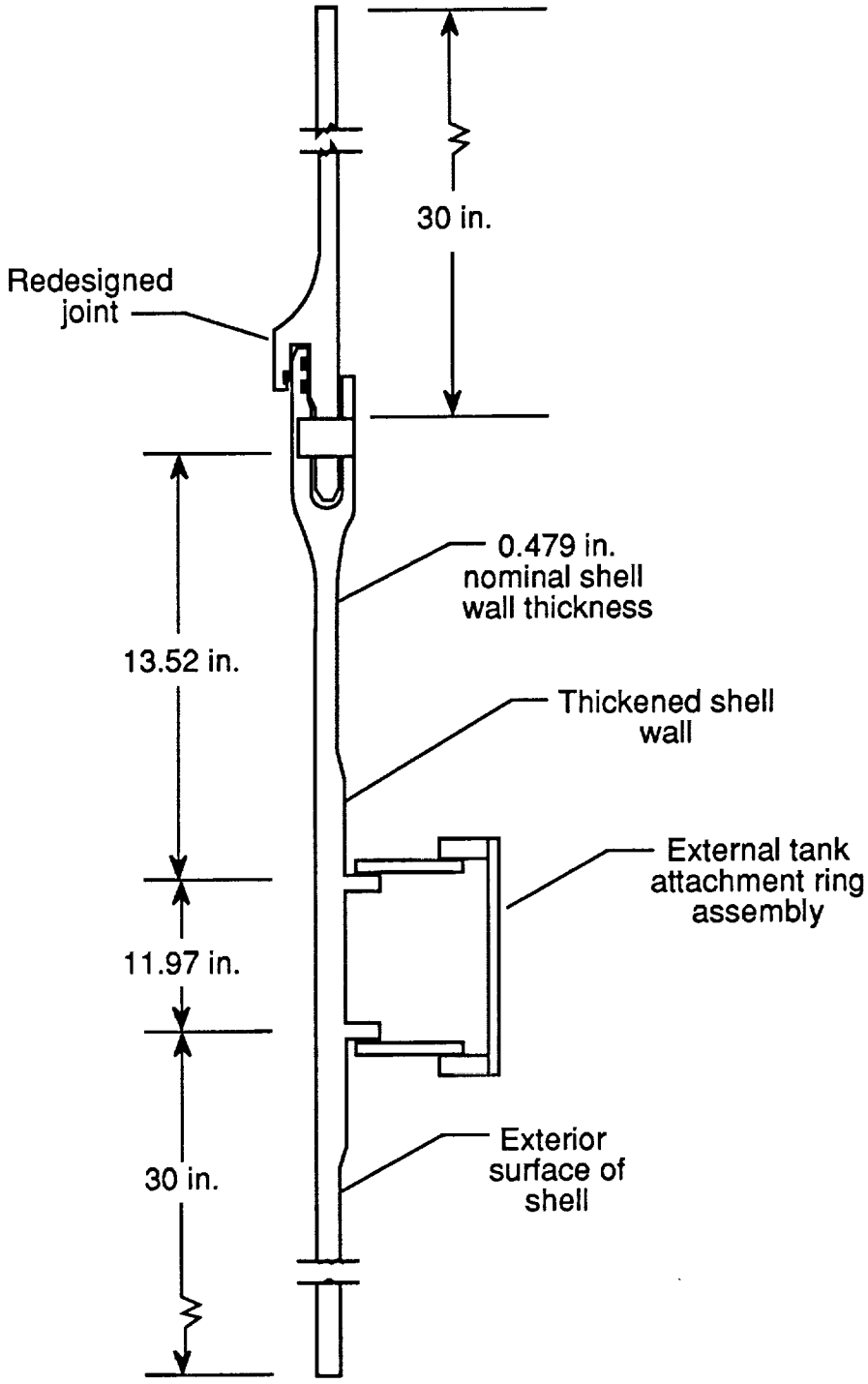


Figure 19. External tank attachment ring assembly and redesigned joint (not to scale).

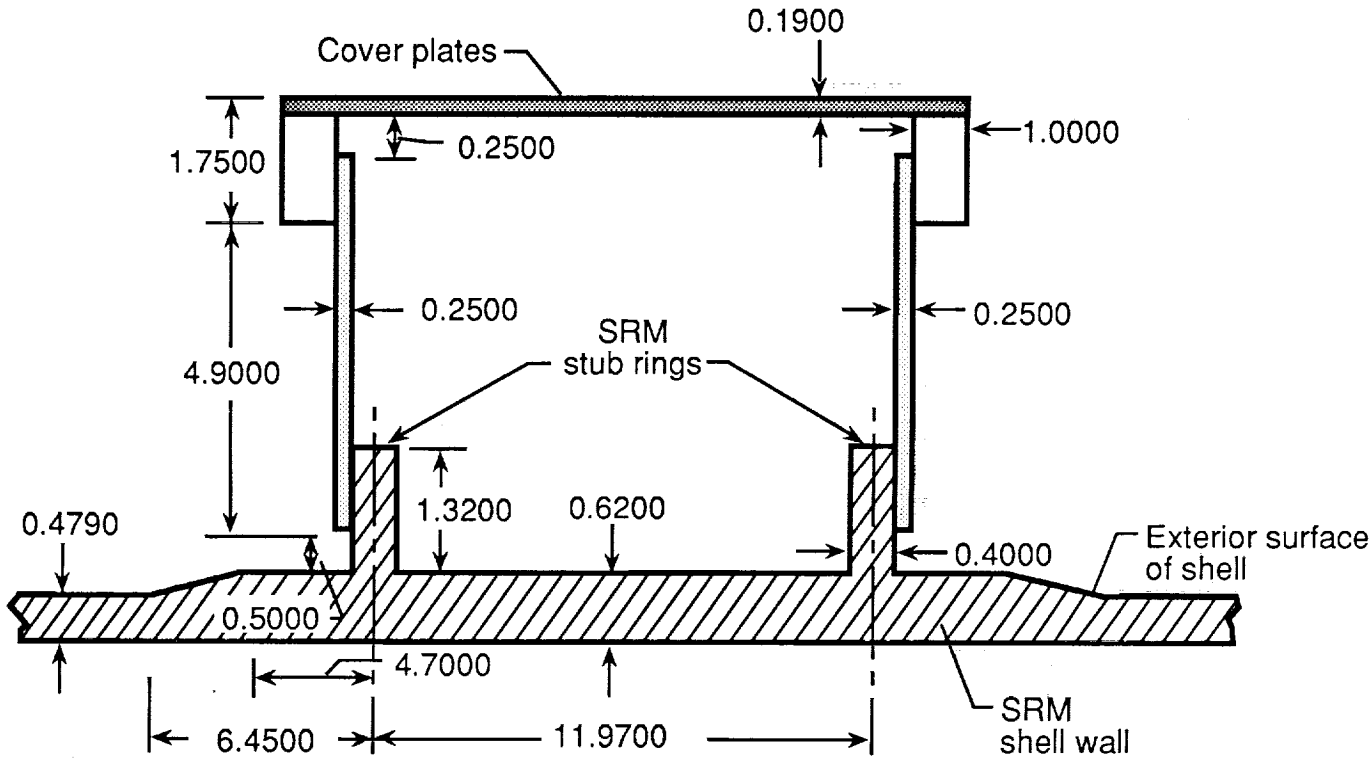


Figure 20. Geometry and dimensions of external tank attachment ring assembly at its largest cross section (not to scale). All dimensions in inches.

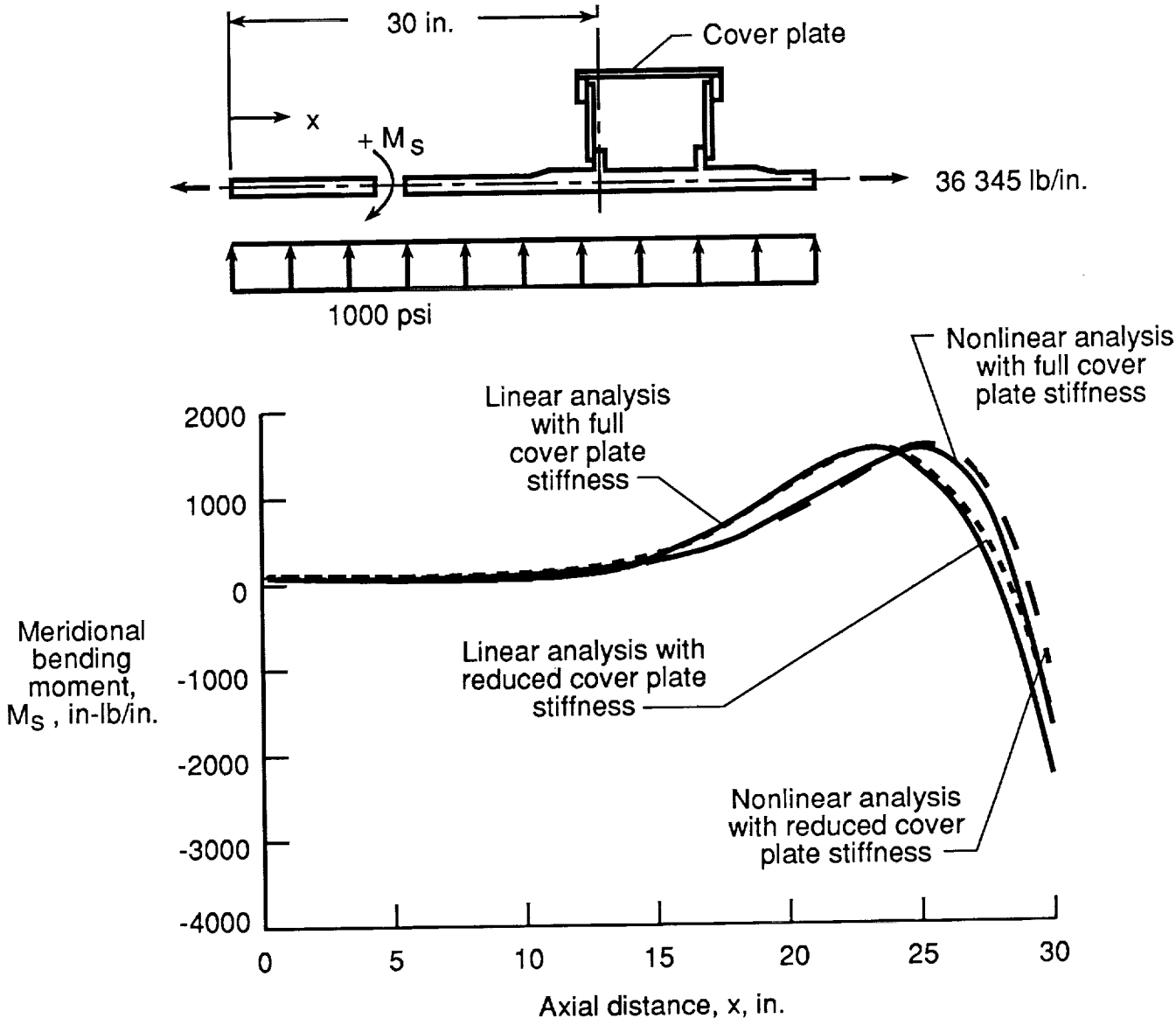


Figure 21. Variation in meridional bending moment with axial distance from external tank attachment ring assembly.

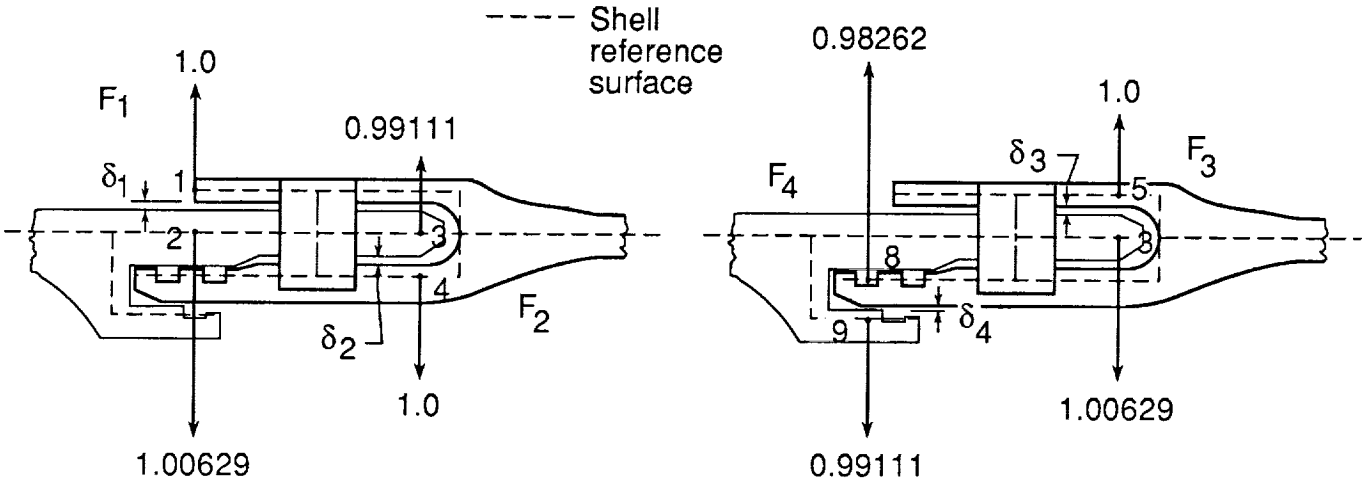


(a) $F_1$ and $F_2$ influence loads.

(b) $F_3$ and $F_4$ influence loads.

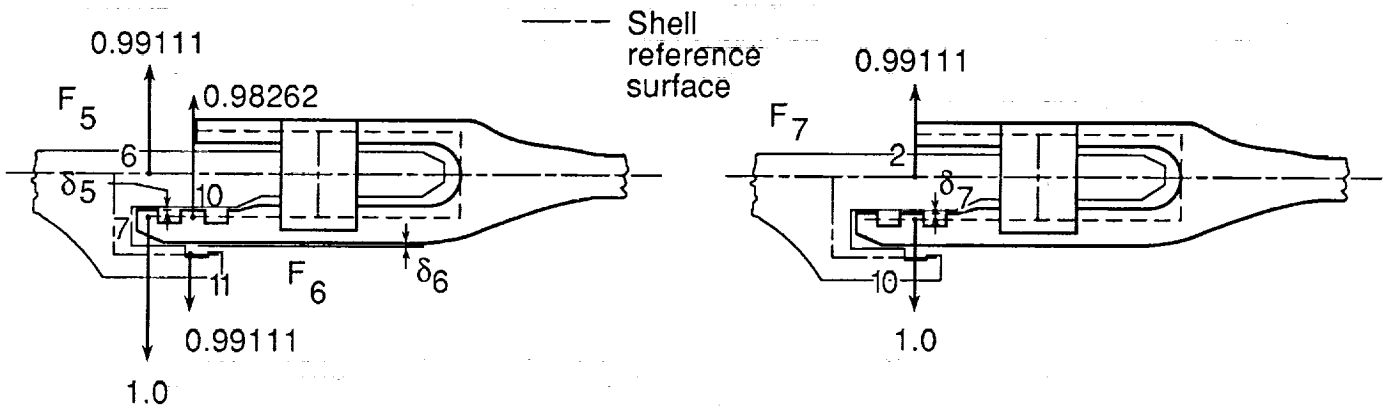


(c) $F_5$ and $F_6$ influence loads.

(d) $F_7$ influence load.

Figure 22. Clearances, nondimensional influence loads, and contact points of redesigned joint.

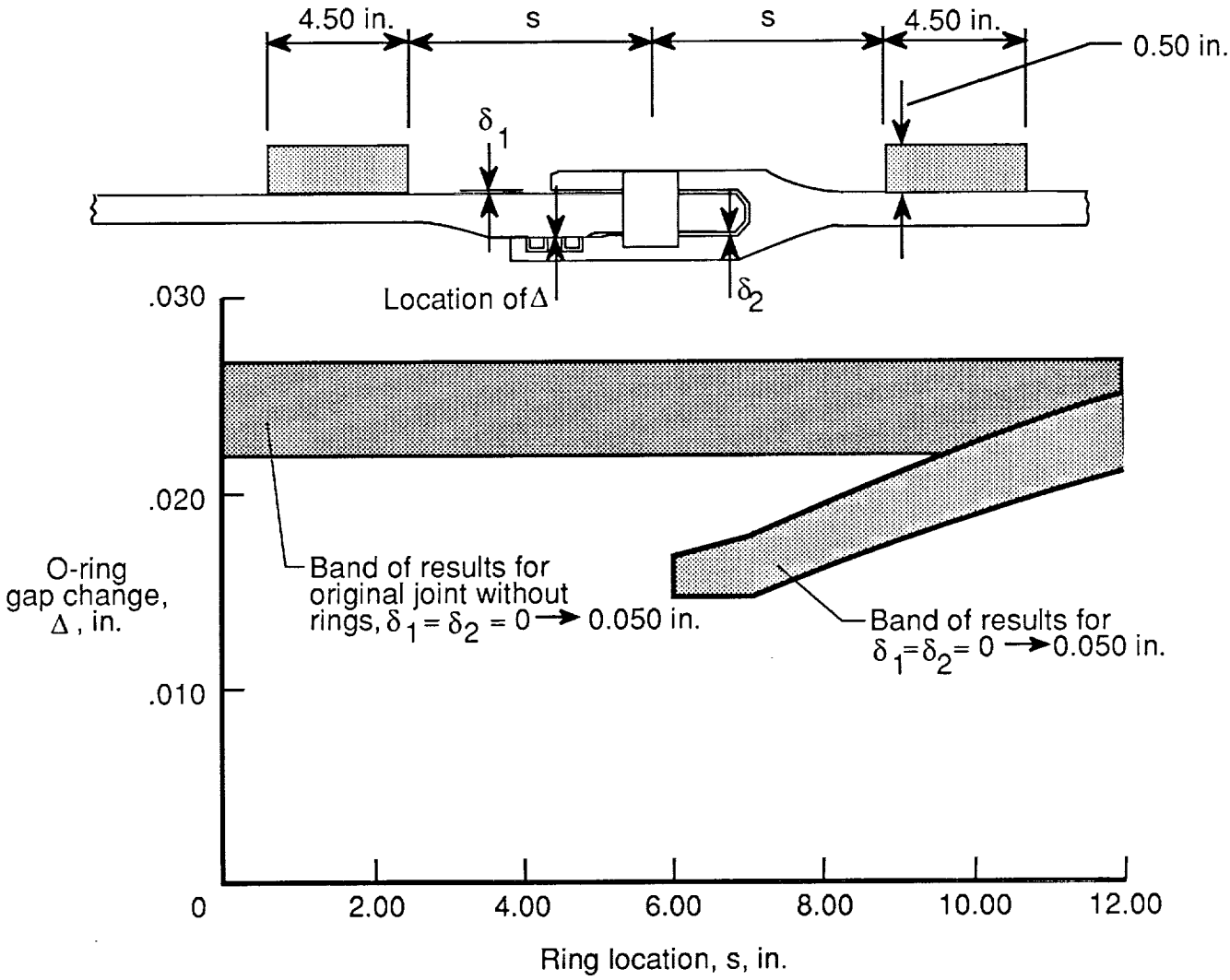


Figure 23. Effects of ring location on O-ring gap changes of original joint modified with two exterior rings. Pressure seal at primary O-ring (1000-psi normal pressure loading).

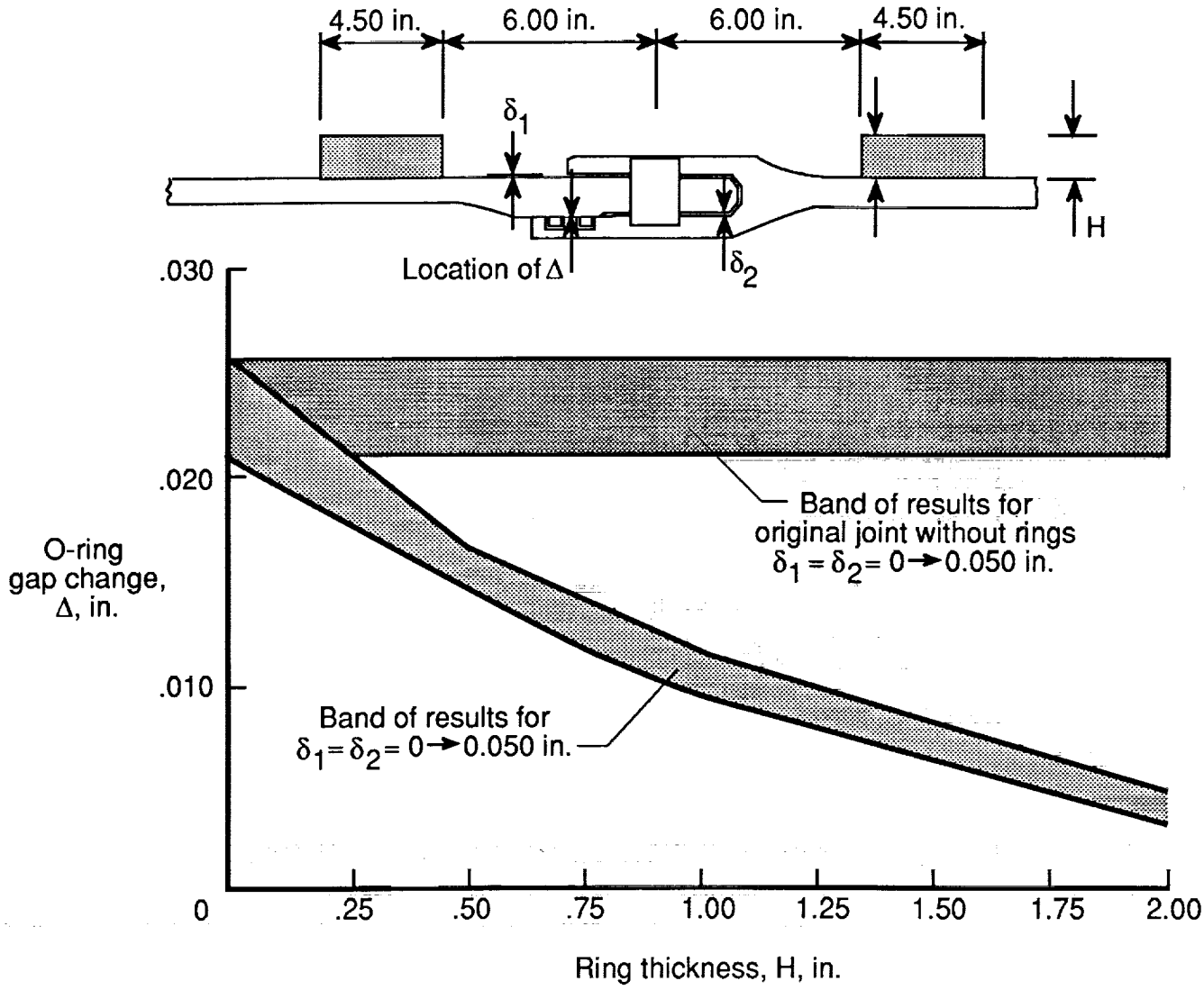


Figure 24. Effects of ring thickness on O-ring gap changes of original joint modified with two exterior rings. Pressure seal at primary O-ring (1000-psi normal pressure loading).

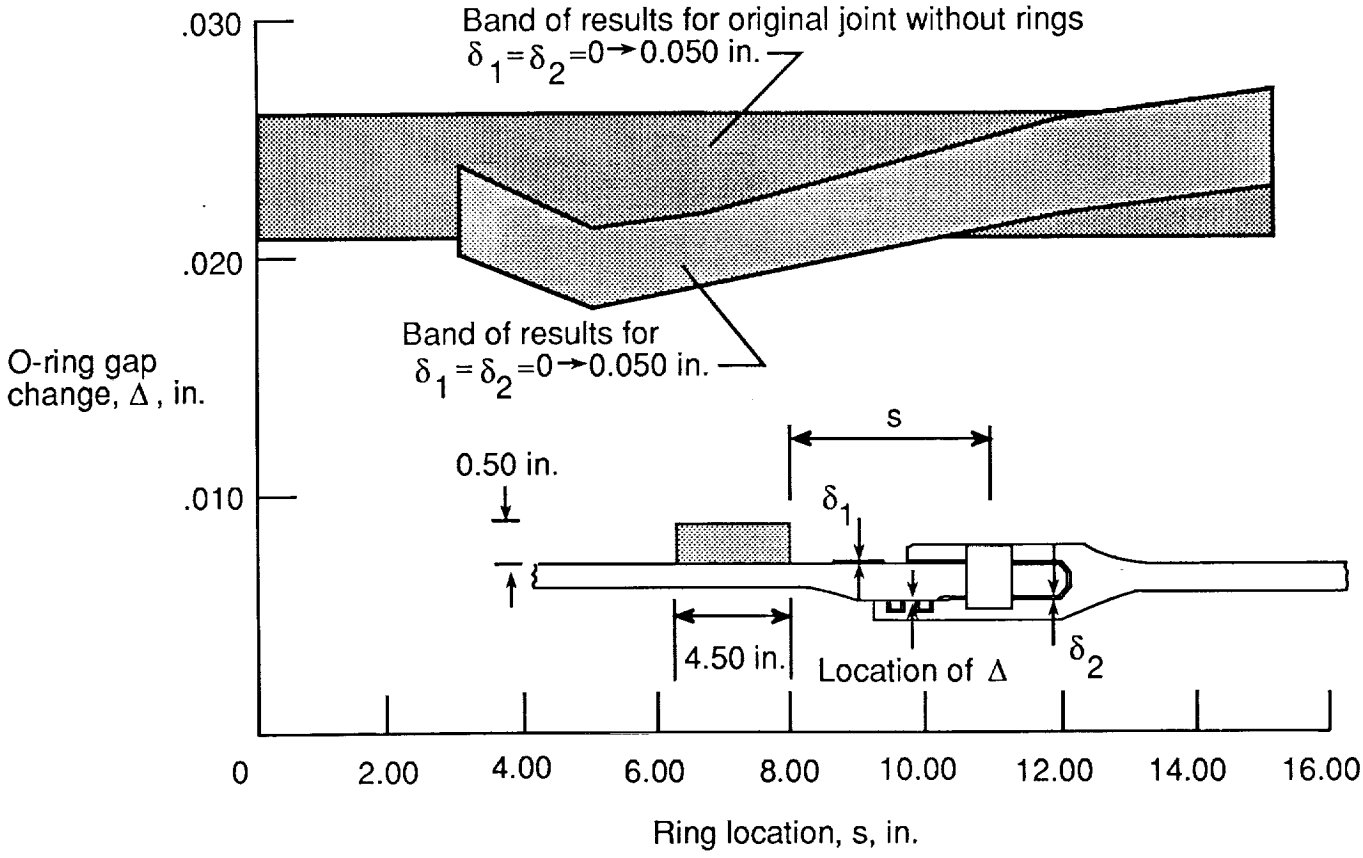


Figure 25. Effects of ring location on O-ring gap changes of original joint modified with one exterior ring. Pressure seal at primary O-ring (1000-psi normal pressure loading).

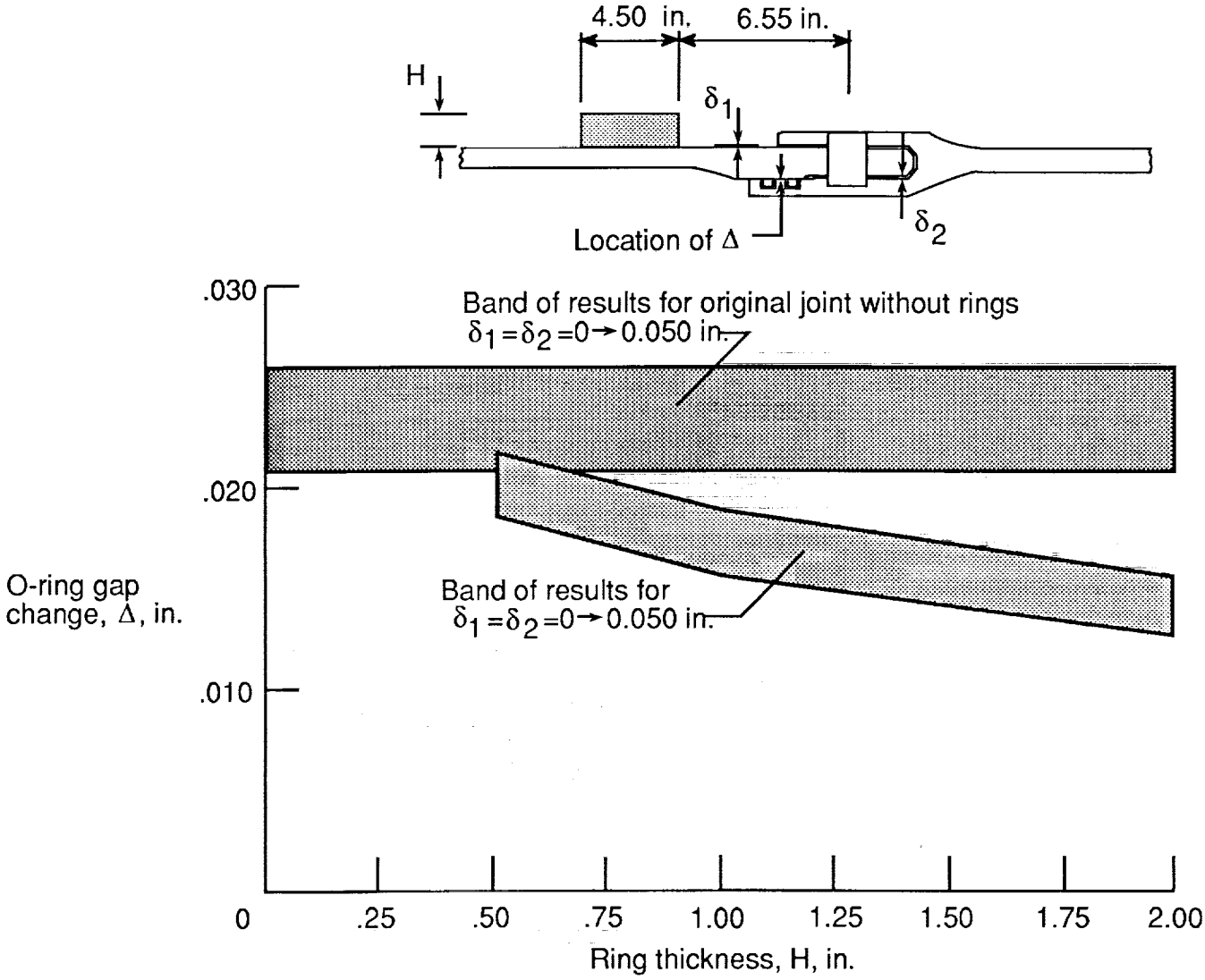


Figure 26. Effects of ring thickness on O-ring gap changes of original joint modified with one exterior ring. Pressure seal at primary O-ring (1000-psi normal pressure loading).

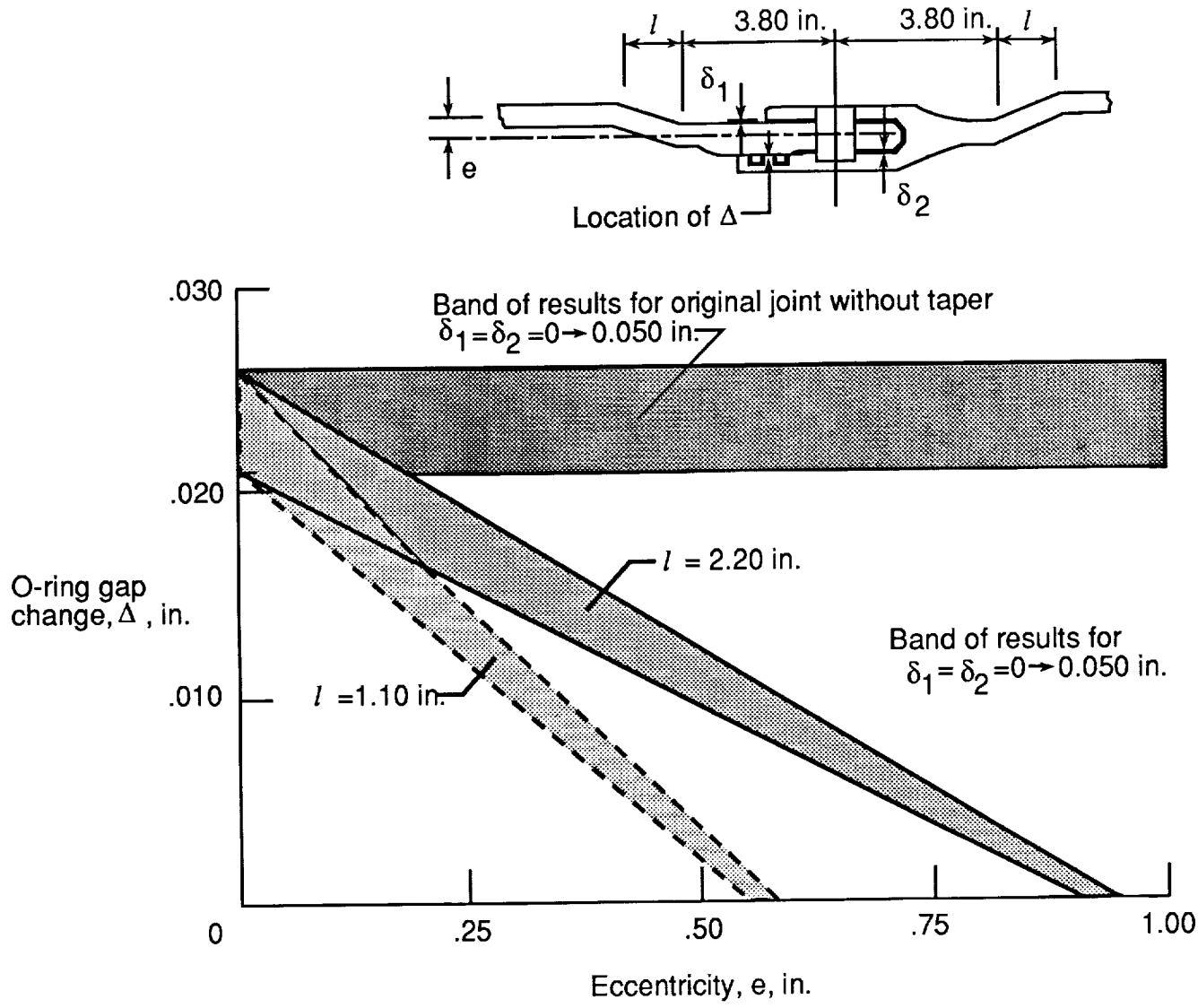


Figure 27. Effects of shell wall eccentricity on O-ring gap changes of modified original joint. Pressure seal at primary O-ring (1000-psi normal pressure loading).

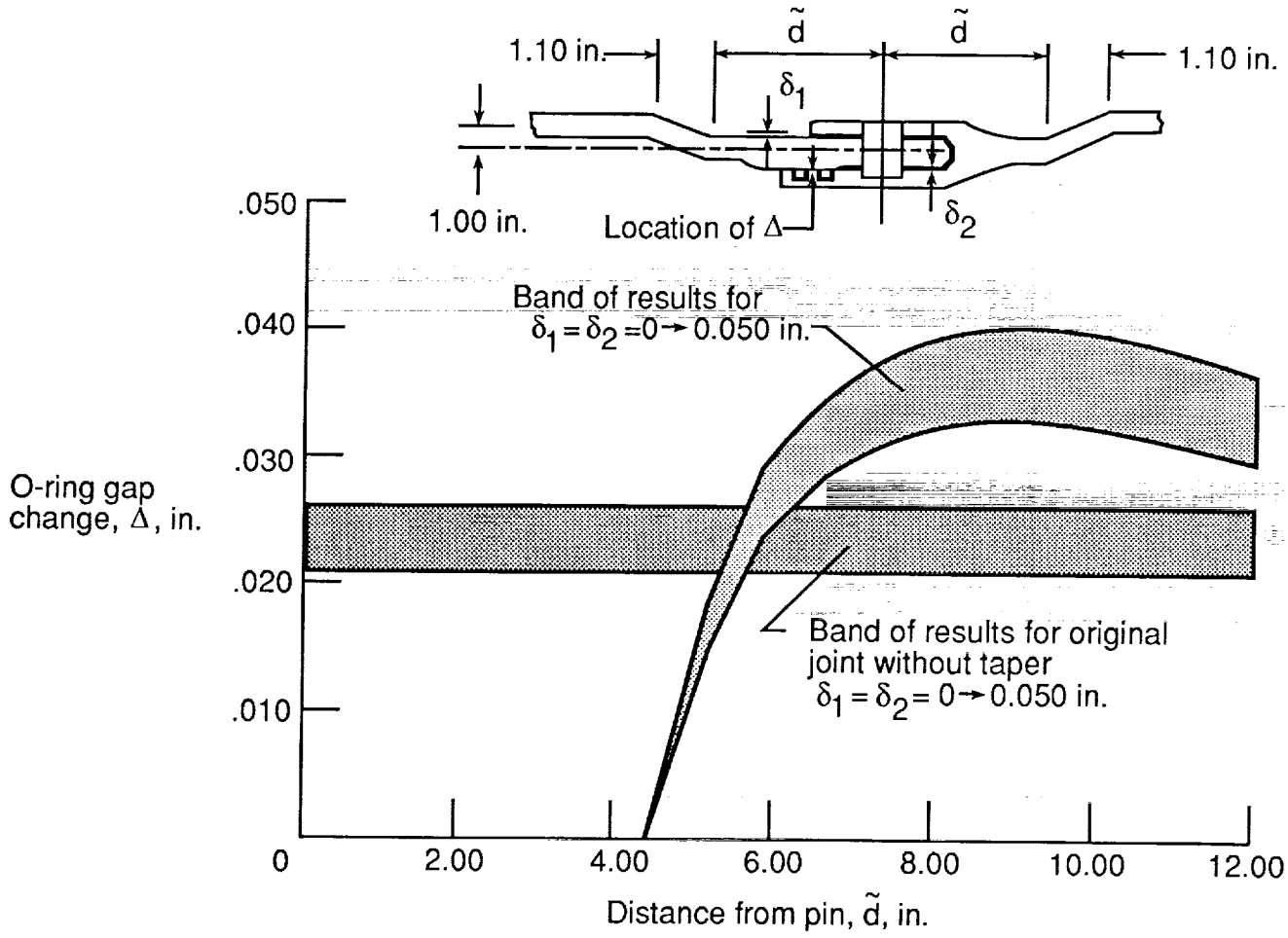


Figure 28. Effects of axial location of shell wall eccentricity on O-ring gap changes of modified original joint. Pressure seal at primary O-ring (1000-psi normal pressure loading).

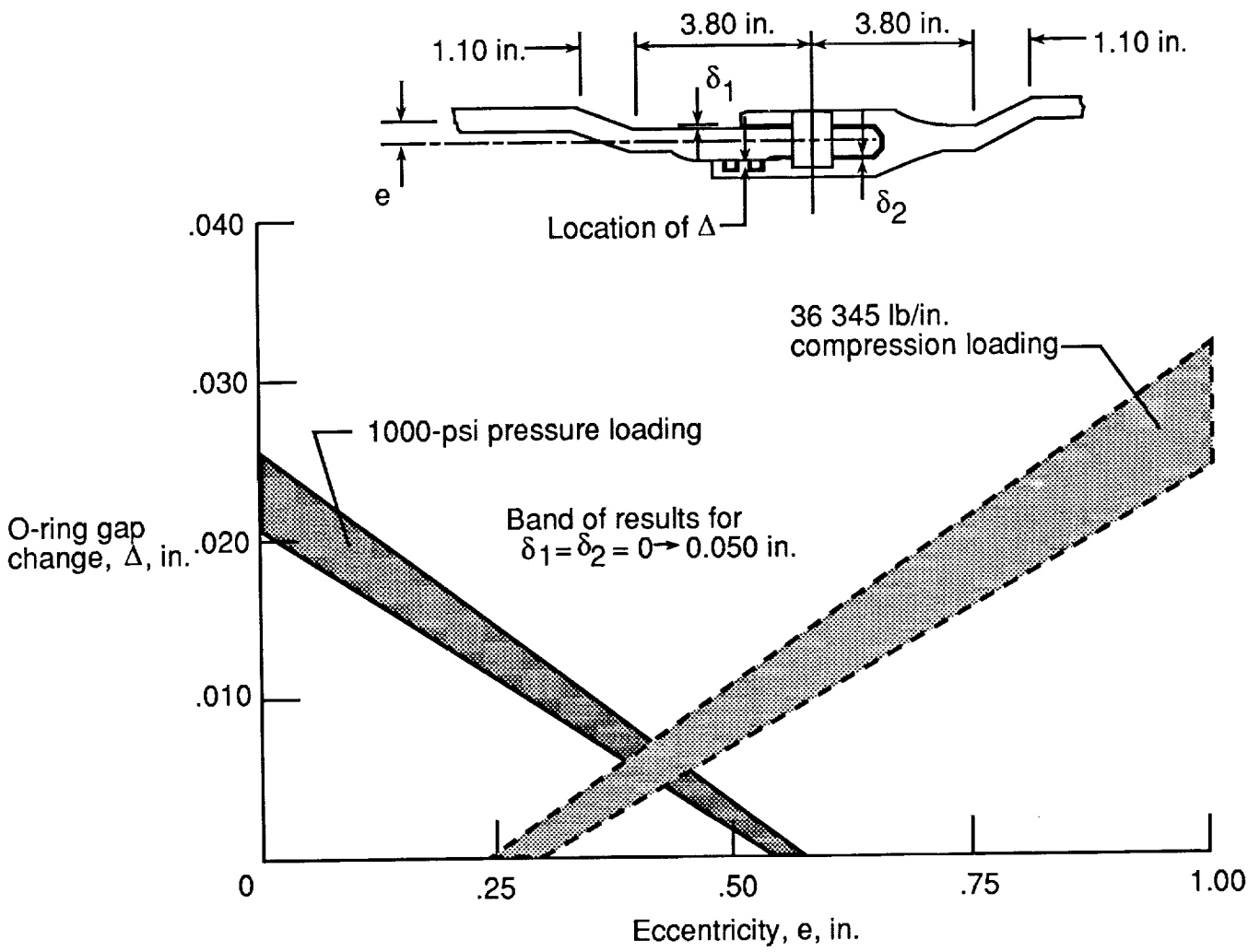


Figure 29. Effects of shell wall eccentricity on O-ring gap changes of modified original joint for internal pressure and axial compression loadings. Pressure seal at primary O-ring.

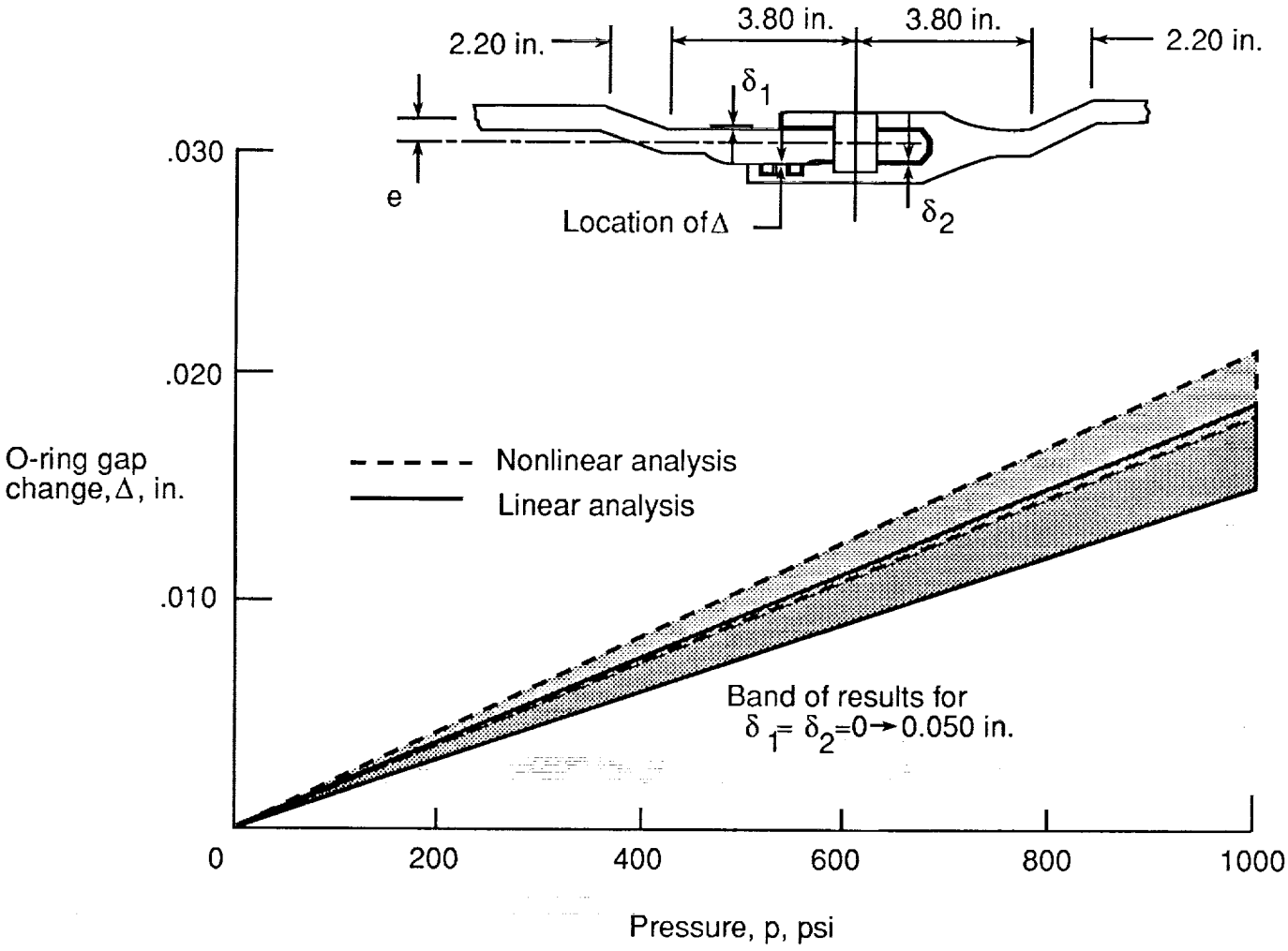


Figure 30. Linear and nonlinear static response of original joint modified with shell wall eccentricity ($e = 0.25$ in.) and subjected to internal pressure.

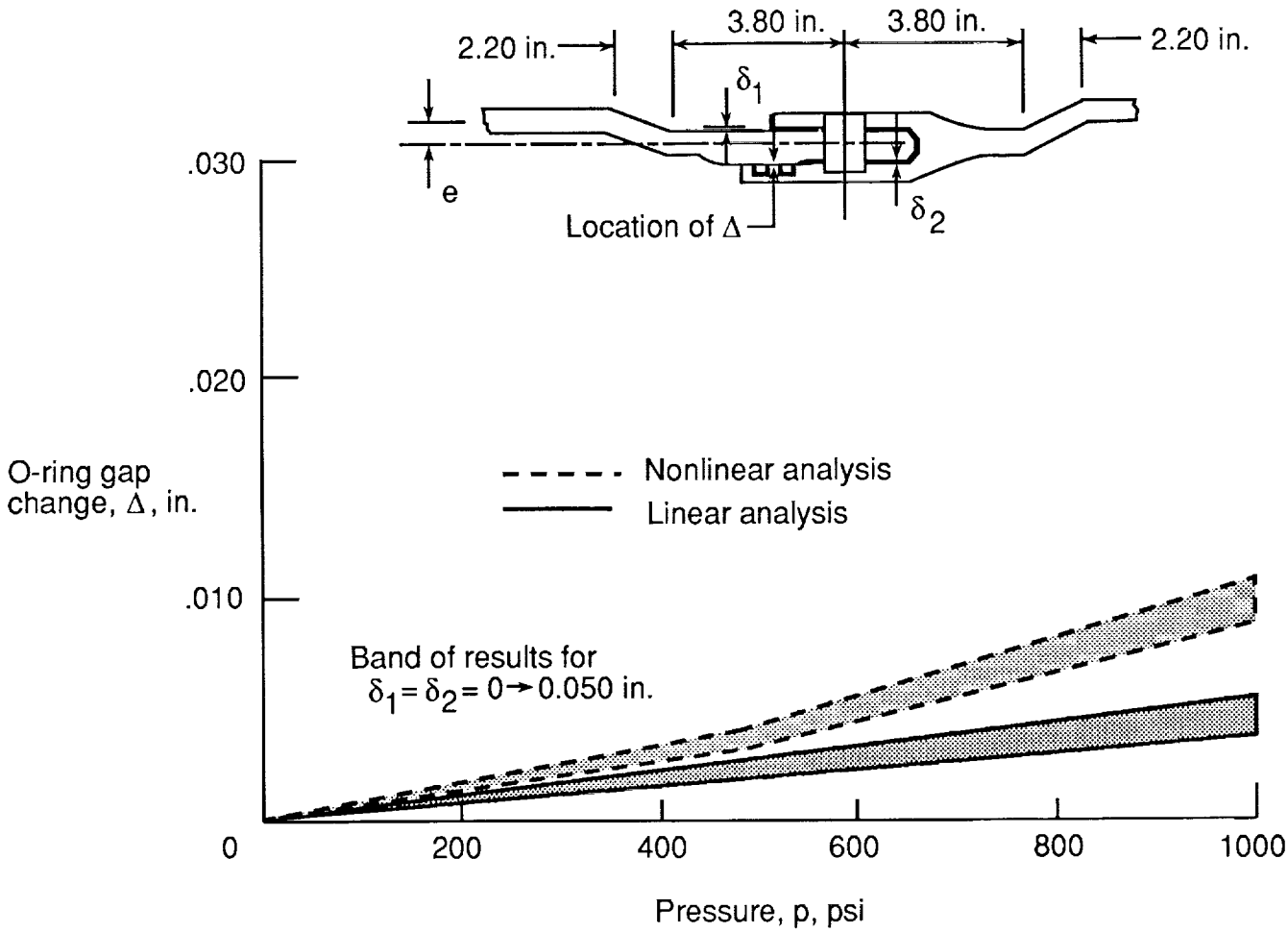


Figure 31. Linear and nonlinear static response of original joint modified with shell wall eccentricity ($e = 0.74$ in.) and subjected to internal pressure.

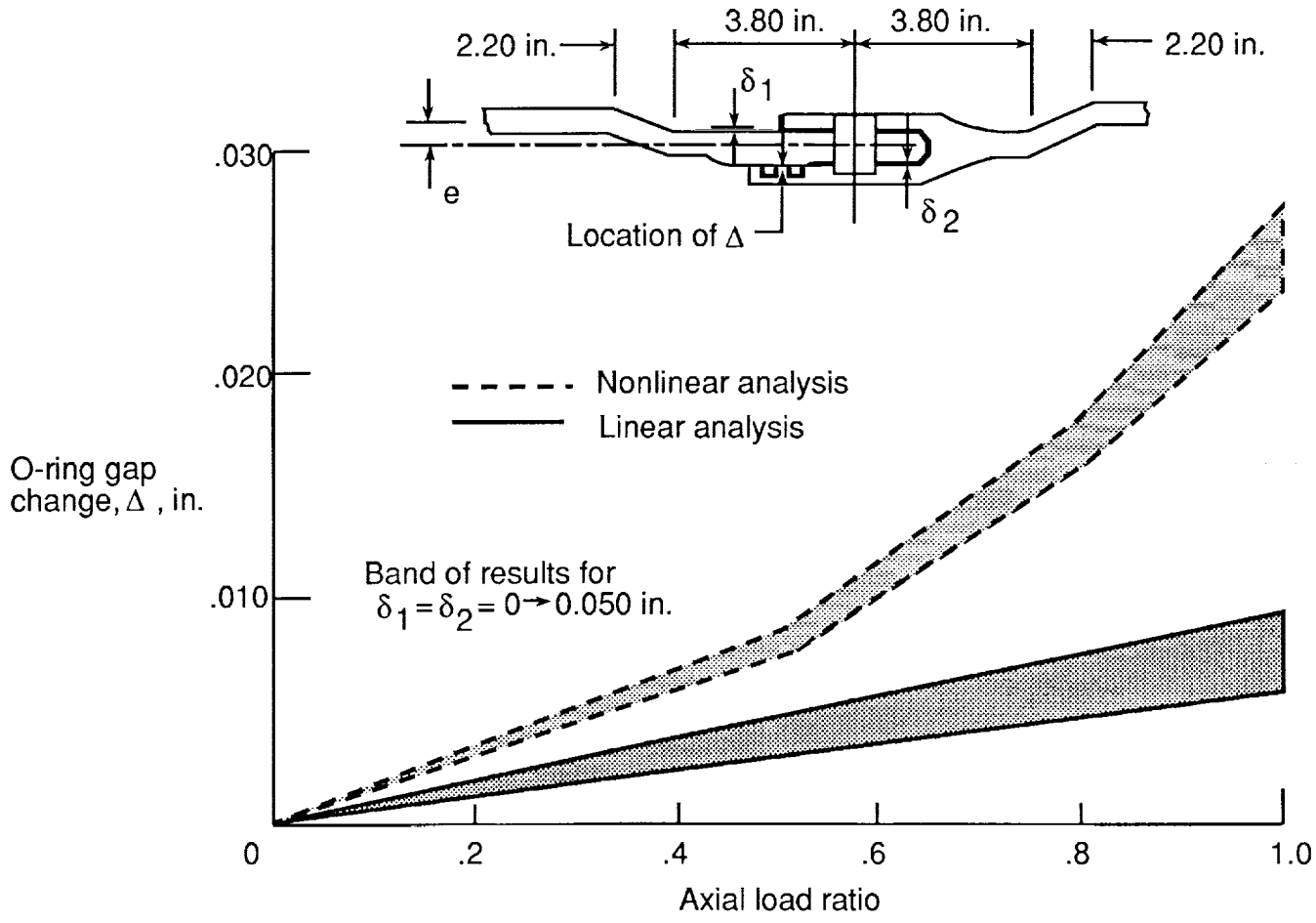


Figure 32. Linear and nonlinear static response of original joint modified with shell wall eccentricity ($e = 0.74$ in.) and subjected to axial compression. Load ratio equals axial load divided by 36 345 lb/in.

NASA
National Aeronautics and Space Administration

# Report Documentation Page

| 1. Report No. | 2. Government Accession No. | 3. Recipient's Catalog No. |
|---|---|---|
| NASA TP-3033 | | |

| 4. Title and Subtitle | 5. Report Date |
|---|---|
| Axisymmetric Shell Analysis of the Space Shuttle Solid Rocket Booster Field Joint | January 1991 |
| | 6. Performing Organization Code |
| 7. Author(s) | 8. Performing Organization Report No. |
| Michael P. Nemeth and Melvin S. Anderson | L-16746 |
| 9. Performing Organization Name and Address | 10. Work Unit No. |
| NASA Langley Research Center<br>Hampton, VA 23665-5225 | 505-63-01-08 |
| | 11. Contract or Grant No. |
| 12. Sponsoring Agency Name and Address | 13. Type of Report and Period Covered |
| National Aeronautics and Space Administration<br>Washington, DC 20546-0001 | Technical Paper |
| | 14. Sponsoring Agency Code |

15. Supplementary Notes

Michael P. Nemeth: NASA Langley Research Center, Hampton, Virginia.
Melvin S. Anderson: Old Dominion University, Norfolk, Virginia.

16. Abstract

The Space Shuttle *Challenger* accident (flight STS-51-L) led to an intense investigation of the structural behavior of the solid rocket booster (SRB) tang and clevis field joints. This paper presents results of axisymmetric shell analyses that parametrically assess the structural behavior of SRB field joints subjected to quasi-steady-state internal pressure loading for both the original joints flown on flight STS 51-L and the redesigned joints flown on the first flight after the accident (on the Space Shuttle *Discovery*). Axisymmetric shell modeling issues and details are discussed and a generic method for simulating contact between adjacent shells of revolution is described. Results are presented that identify the performance trends of the joints for a wide range of joint parameters. The redesigned joint exhibits significantly smaller O-ring gap changes and much less sensitivity to joint clearances than the original joint. For a wide range of joint parameters, the results presented in this study indicate that the redesigned joint provides a much better pressure seal than the original joint.

| 17. Key Words (Suggested by Authors(s)) | 18. Distribution Statement |
|---|---|
| Solid rocket booster<br>Axisymmetric<br>Shell analysis<br>Parameters | Unclassified—Unlimited<br><br>Subject Category 39 |

| 19. Security Classif. (of this report) | 20. Security Classif. (of this page) | 21. No. of Pages | 22. Price |
|---|---|---|---|
| Unclassified | Unclassified | 53 | A04 |



For sale by the National Technical Information Service, Springfield, Virginia 22161-2171